Geophysical Journal International

Geophys. J. Int. (2024) **237,** 465–484 https://doi.org/10.1093/gji/ggae052
Advance Access publication 2024 February 10
GJI Geomagnetism and Electromagnetism

Remagnetization of the Upper Permian–Lower Triassic limestones in the western Lhasa Terrane and its tectonic implications

Weiwei Bian,[1,2] Xianwei Jiao,[1] Suo Wang,[1] Jiacheng Liang,[1] Jiahui Ma,[1] Jikai Ding,[1] Hanqing Zhao,[1] Tianshui Yang,[1] Shihong Zhang,[1] Huaichun Wu,[1] Haiyan Li[1] and Chenglong Deng[2]

[1]*State Key Laboratory of Biogeology and Environmental Geology, China University of Geosciences, Beijing* 100083*, China. E-mail: bianww@cugb.edu.cn*
[2]*State Key Laboratory of Lithospheric Evolution, Institute of Geology and Geophysics, Chinese Academy of Sciences, Beijing* 100029*, China*

Accepted 2024 February 9. Received 2024 January 30; in original form 2023 August 27

SUMMARY

The drift history of the Lhasa terrane plays an essential role in understanding the tectonic evolution of the Bangong-Nujiang Tethyan Ocean and the Neo-Tethyan Ocean, as well as the evolutionary history of the Tibetan Plateau. Here, a combined rock magnetic, petrographic, and palaeomagnetic study is performed on the Upper Permian–Lower Triassic limestones (∼259–251 Ma) in the western Lhasa terrane. The site-mean direction for the 28 sites is $D_g = 32.1°$, $I_g = 50.3°$, $k_g = 47.9$ and $\alpha_{95} = 4.0°$ *in situ* and $D_s = 342.9°$, $I_s = 32.7°$, $k_s = 43.2$ and $\alpha_{95} = 4.2°$ after tilt-correction, yielding a palaeopole at 68.9°N, 314.4°E with $A_{95} = 4.3°$, corresponding to a palaeolatitude of 18.0° ± 4.3°N. The fold tests are not significant because the sampling section shows monoclinic features with minor variations in their bedding attitudes. The palaeopoles for the directions before and after tilt-correction are compared with reliable Late Permian–Palaeogene palaeopoles obtained from the Lhasa terrane. Based on these comparisons, the studied limestones were remagnetized prior to tilting and this remagnetization most likely occurred during the Early Cretaceous. The depositional environment of the limestones may have changed from anoxic to suboxic and oxic during the Early Cretaceous, leading to the oxidation of iron sulphide to authigenic magnetite. Meanwhile, the Late Jurassic–Early Cretaceous convergence between the western Lhasa and Qiangtang terranes may have resulted in tectonic fluid migration and the formation of calcite veins and stylolites in the limestones. This is supported by the presence of small calcite veins and stylolites in some samples, as well as the fact that the framboidal oxides were formerly sulphides (mostly pyrite), implying that the majority of the iron oxides observed in the limestones were authigenic. These processes indicate that chemical remanent magnetization caused by the growth of magnetic minerals related to tectonic fluid migration was most likely the mechanism for the limestone remagnetization.

Key words: Palaeomagnetism; Remagnetization; Rock and mineral magnetism.

1 INTRODUCTION

The Tibetan Plateau, known as the roof of the world, formed from a complex tectonic collage of multiple continental fragments, including the Himalaya, Lhasa, Qiangtang, Songpan-Ganzi and Kunlun-Qaidam from south to north (Fig. 1). The northward motion of these continental fragments has involved various types of tectonic activities, including the continental breakup, drift, subduction, collision, accretion and evolution of the Tethyan oceans (Yin & Harrison 2000; Zhu *et al.* 2013; Hu *et al.* 2016, 2022; Kapp *et al.* 2019). Those processes have had long-term impacts on the global palaeogeography, palaeoclimate and palaeoecology (Raymo & Ruddiman 1992; Guo *et al.* 2002; Chatterjee *et al.* 2013; van Hinsbergen *et al.* 2018; Li *et al.* 2019; Su *et al.* 2019; Yuan *et al.* 2021, 2022; Deng *et al.* 2023). The Lhasa terrane was separated from the Qiangtang terrane to the north by the Bangong-Nujiang suture zone and from the Tethyan Himalaya to the south by the Indus-Yarlung Tsangpo suture zone (Fig. 1). Therefore, the drift history of the Lhasa terrane is vital to understanding the evolution of the Bangong-Nujiang Tethyan Ocean and the Neo-Tethyan Ocean.

Palaeomagnetism is a powerful technique to quantify plate palaeogeography and is therefore valuable for constraining the kinematic processes of plate movement (Appel *et al.* 1998; Liebke *et al.* 2010; Yi *et al.* 2011; van Hinsbergen *et al.* 2012; Lippert *et al.*

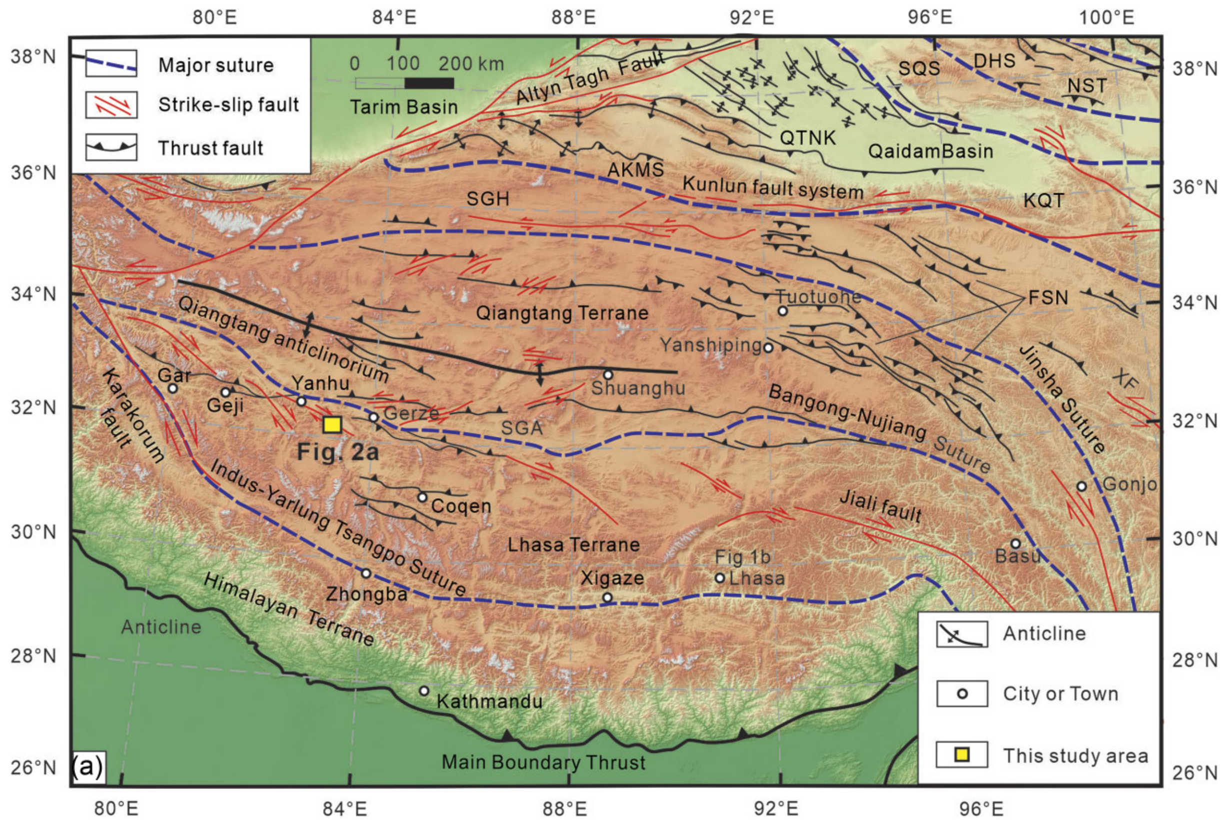

Figure 1. Tectonic sketch of the Tibetan Plateau and adjacent areas modified after Wang *et al.* (2023). Abbreviations: AKMS, Ayimaqin-Kunlun-Muztagh suture; DHS, Danghe Nan Shan suture; FSN, Fenghuo Shan-Nangqian fold and thrust belt; KQT, Kunlun-Qaidam terrane; QTNK, Qimen Tagh-North Kunlun thrust system; NQS, North Qilian Suture; NST, Nan Shan thrust belt; SGA, Shiquanhe-Gaize-Ando thrust system; SGH, Songpan-Ganzi-Hoh Xil terrane and SQS, South Qilian suture.

2014; Yang *et al.* 2015b; Yan *et al.* 2016; Chen *et al.* 2017; Bian *et al.* 2019, 2021; Ma *et al.* 2019; Cao *et al.* 2020; Song *et al.* 2020; Jadoon *et al.* 2022; Jiao *et al.* 2023). Many palaeomagnetic studies have been conducted on the Late Palaeozoic–Mesozoic strata of the Lhasa terrane to constrain its drift history. However, most palaeomagnetic datasets have come from Cretaceous strata (Pozzi *et al.* 1982; Lin & Watts 1988; Chen *et al.* 1993, 2012; Sun *et al.* 2008, 2012; Tan *et al.* 2010; Ma *et al.* 2014, 2022a; Yi *et al.* 2015; Yang *et al.* 2015a; Tong *et al.* 2017; Liu *et al.* 2022; Cao *et al.* 2023; Niu *et al.* 2023) and only a few are derived from Late Palaeozoic–Early Mesozoic strata (Ran *et al.* 2012; Cheng *et al.* 2015; Zhou *et al.* 2016). Zhou *et al.* (2016) reported an Early–Middle Triassic palaeopole (18.9°N, 208.4°E, $A_{95} = 3.9°$) and a Late Triassic palaeopole (19.6°N, 211.8°E, $A_{95} = 10.7°$) from 47 and 37 marine sedimentary specimens, respectively. Their results indicate that the Lhasa terrane maintained a relatively stable palaeolatitude (∼16.5–18.4°S) throughout the Triassic. Cheng *et al.* (2015) obtained a Triassic palaeopole (17.4°N, 205.9°E, $dp/dm = 6.7°/3.7°$) from 28 marine sedimentary specimens, indicating that the Lhasa terrane was located at ∼15.7°S during the Triassic. Ran *et al.* (2012) reported Permian and Late Triassic sedimentary palaeomagnetic results from the Lhasa terrane. Their results indicate that the Lower Permian Angjie Formation sandstones (11 specimens) preserve the primary magnetization, whereas the Middle Permian Xiala Formation limestone (35 specimens), the Upper Permian Mujiucuo Formation dolomite (34 specimens) and the Upper Triassic Duoburi Formation silicalite (11 specimens) suffered from remagnetization. Because of the scarcity of Late Palaeozoic–Early Mesozoic palaeomagnetic data and the widespread remagnetization (Ran *et al.* 2012), it is still difficult to accurately constrain the Late Palaeozoic–Early Mesozoic palaeogeography of the Lhasa terrane.

The Cuoqin Basin is located to north of the Lhasa terrane, where Permian–Cretaceous marine carbonate and clastic rocks are widely exposed (Ji *et al.* 2018). The Wenbudangsang section in Geji County, located in the central western part of the Cuoqin Basin, is a newly discovered continuous marine carbonate sequence that crosses the Permian–Triassic boundary (Zhou 2012; Wu *et al.* 2014; Ji *et al.* 2019). Conodont biostratigraphy provides a valuable chronological basis for regional stratigraphic correlation and classification (Wu *et al.* 2014) and therefore palaeomagnetic studies. However, carbonate rocks are prone to pervasive remagnetization, especially in orogenic belts, such as those in North America (McCable & Elmore 1989), Europe (Weil & Van der Voo 2002) and the Tibetan Plateau (Appel *et al.* 1998, 2012; Li *et al.* 2020; Fu *et al.* 2022). Remagnetization can obscure or remove primary magnetization and can occur pre-folding (Huang *et al.* 2015; Zhang *et al.* 2016; Xu *et al.* 2022), syn-folding (Ran *et al.* 2017; Huang *et al.* 2017a, b) or post-folding (Cao *et al.* 2019; Gao *et al.* 2019; Zhang *et al.* 2020). Therefore, caution is required when using paleomagnetism for carbonate rocks from orogenic belts.

This paper presents a combined rock magnetic, petrographic and palaeomagnetic study on Upper Permian–Lower Triassic limestones from the Wenbudangsang section of the Lhasa terrane. We evaluate the timing of the remanence acquisition and discuss potential remagnetization acquisition mechanisms and their tectonic implications.

2 GEOLOGICAL BACKGROUND AND SAMPLING

The study area (Wenbudangsang section) is located in the Wenbudangsang area of the western Lhasa terrane, ∼180 km southeast of Geji County. In the 1:250 000 Wuma regional geological map (I44C004004 2006), the sampled limestones in the Wenbudangsang area are assigned to the Lower Permian Xiala Formation. The Xiala Formation conformably overlies the Upper Carboniferous Laga Formation and unconformably underlies the Lower Cretaceous strata. This formation mainly occurs on the southern side of the Nianle-Maijue fault and/or the Jienisuola-Lagala fault. These two faults developed primarily during the Late Yanshanian–Early Himalayan periods (I44C004004 2006). The unconformity between the Xiala Formation strata and the Lower Cretaceous strata indicates that the folding of the Xiala Formation strata likely occurred before or during the Early Cretaceous.

However, new conodont index species indicate that the sampled limestones should be assigned to the Upper Permian Wenbudangsang Formation and the Lower Triassic Garencuo Formation (Wu *et al.* 2014). The Wenbudangsang Formation primarily consists of grey limestones with rich cherty nodules or layers and formed in a marine carbonate slope depositional environment (Wu *et al.* 2014). The Garencuo Formation conformably overlies the Wenbudangsang Formation and is primarily composed of limestones with rare siliceous nodules or chert beds (Zhou 2012; Wu *et al.* 2014). Based on biostratigraphy and lithostratigraphy, the Garencuo Formation was deposited in a carbonate platform slope environment (Ji *et al.* 2007).

To avoid confusion, the new nomenclature (i.e. the Wenbudangsang and Garencuo formations) was adopted in this study. In total, 293 core samples from 29 palaeomagnetic sites were collected near the village of Wenbudangsang (32°16′5.1″–32°16′9.9″N, 83°1′17.8″–83°1′44.0″E; Fig. 2). Of these, 21 sites sampled the Garencuo Formation (WB1–WB21) and 8 sites sampled the Wenbudangsang Formation (WB22–WB29). The bedding attitudes of the Wenbudangsang and Garencuo formations (dipped 40°–63° towards the northwest) are clear (Fig. 3). In general, 10 oriented samples were collected from each site, spanning several meters in stratigraphic thickness.

Samples were collected using a portable gasoline-powered drill. Cores were oriented with a magnetic compass and, when possible, a solar compass. The differences between these two orienting methods range from 1.1° to 5.4°. When the solar compass was unavailable, the mean value (3.79°) was used to correct the orientation of the samples.

3 ROCK MAGNETIC RESULTS

To identify magnetic minerals, hysteresis loops, acquisition curves of the isothermal remanent magnetization (IRM), back-field demagnetization of the saturation IRM (SIRM), thermomagnetic curves (k–T curves) and thermal demagnetization of the three-axis IRM (Lowrie 1990) were measured for representative specimens. The acquisitions of the IRM, back-field demagnetization of the SIRM and thermal demagnetization of the three-axis IRM for five specimens were performed using an ASC IM10-30 pulse magnetizer and were measured using a JR-6A spinner magnetometer and a 2 G 755–4 K cryogenic magnetometer at the Palaeomagnetism and Environmental Magnetism Laboratory (PMEML), Beijing. The demagnetization diagram served as the primary criterion for selecting specimens. The specimens were fully demagnetized at ∼80 mT (WB28), ∼100 mT (WB8) and ∼120 mT (WB17) and were not completely demagnetized at ∼120 mT (WB21). The three-axis IRM was applied successively at fields of 2.4, 0.4 and 0.12 T along three mutually orthogonal axes. Measurements of the k–T curves were made on nine fresh powder samples in an argon environment using a KLY-3S Kappabridge combined with a CS-3 high-temperature furnace at PMEML. Hysteresis loops and back-field curves for the nine samples were measured to determine the saturation magnetization (M_s), saturation remanent magnetization (M_{rs}), coercivity force (B_c) and remanent coercivity (B_{cr}) using a MicroMag^{TM} Model 3900 Vibrating Sampling Magnetometer at the Palaeomagnetism and Geochronology Laboratory of the Institute of Geology and Geophysics, China Academy of Sciences (IGGCAS), Beijing. Hysteresis loops were measured with a maximum applied field of 0.3 T, and a slope correction was applied at 70 per cent of the maximum applied field. The automatic fitting of the MATLAB program HystLab (Paterson *et al.* 2018) was used to process and analyse the loop data.

The hysteresis loops of the Garencuo and Wenbudangsang formation limestones are open and saturate by 300 mT (Fig. S1). The loops are not typically wasp-waisted as is often seen in remagnetized limestones (Channell & McCabe 1994; McCabe & Channell 1994; Font *et al.* 2012; Huang *et al.* 2015, 2019; Fu *et al.* 2022; Yu *et al.* 2022). Their pot-bellied shape suggests a finer superparamagnetic magnetite assemblage (Pick & Tauxe 1994). On the Day plot (Day *et al.* 1977; Dunlop 2002), all of the samples are located within the pseudosingle domain, with B_{cr}/B_c and M_{rs}/M_s ratios ranging from 1.97 to 2.79 and from 0.17 to 0.34, respectively (Fig. 4 and Table S1). Day plots are widely used to distinguish remagnetized and non-remagnetized carbonate rocks (Jackson & Swanson-Hysell 2012). Some of the hysteresis data of the Upper Permian–Lower Triassic limestones are close to the 'non-remagnetized trend' on the Day-plot, while the remainder overlaps with some remagnetized Jurassic limestones from the eastern Qiangtang terrane (Fig. 4; Fu *et al.* 2022). Likewise, the Middle Jurassic limestones of the Tethyan Himalaya preserve a primary remanent magnetization (Jiao *et al.* 2023). Although the hysteresis data of the 22 limestones are close to the 'non-remagnetized trend', 5 limestones are close to the 'remagnetized trend' on the Day-plot (Jiao *et al.* 2023). Roberts *et al.* (2018) discussed 10 issues that limit the interpretation of a Day plot, and uncertainties tend to complicate interpretations.

The IRM acquisition curves of the Garencuo Formation limestone present a rapid increase below 200 or 300 mT and a gradual increase prior to 2.5 T (Figs 5a–c). The backfield demagnetization of the SIRM curves show a rapid decrease to zero between ∼110 and ∼50 mT (Figs 5a–c). The IRM acquisition curve of the Wenbudangsang Formation limestone exhibits a rapid increase below 200 mT, and saturation was not reached at 2.5 T (Fig. 5d). The backfield demagnetization of the SIRM curve displays a rapid decrease prior to 200 mT and a decrease to zero between 900 and 1000 mT (Fig. 5d). These results indicate that the Garencuo and Wenbudangsang formation limestones contain both low- and high-coercivity magnetic minerals.

The IRM component analyses (Figs 5e–h) display three-humped components: (1) soft component 1 with $B_{1/2}$ (the field when half of the SIRM is acquired) of ∼50–80 mT (constituting 56–66 and 21 per cent of the SIRM for the Garencuo and Wenbudangsang formations, respectively); (2) hard component 2 with $B_{1/2}$ of ∼2000–2240 mT (constituting 14–34 and 74 per cent of the SIRM for the Garencuo and Wenbudangsang formations, respectively) or ∼250 mT (constituting 16 per cent of the SIRM for the Garencuo Formation) and (3)

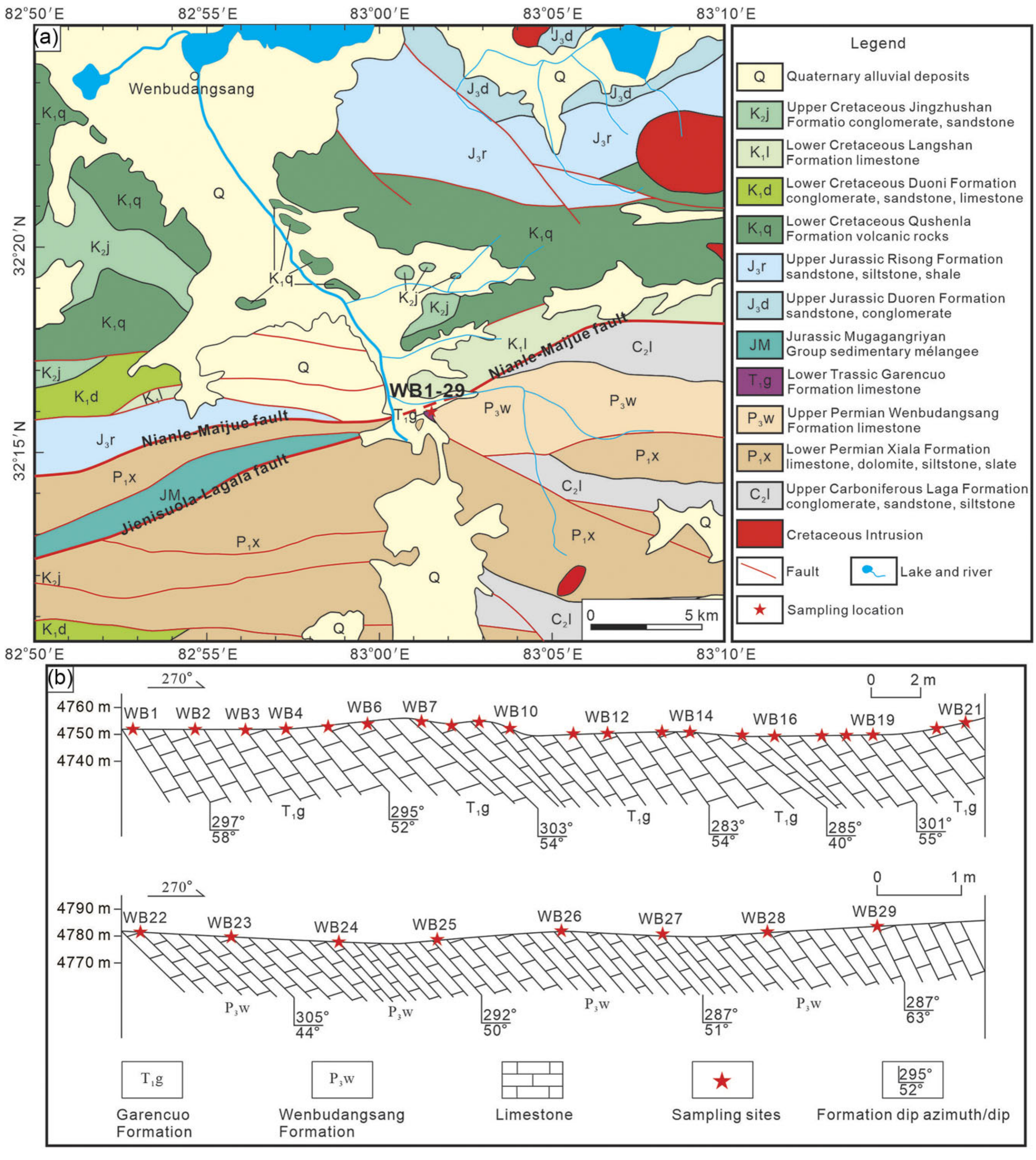

Figure 2. (a) Simplified geological map of the study area. (b) Cross section of the sampled Garencuo and Wenbudangsang formation limestones in the Wenbudangsang area.

hard component 3 with $B_{1/2}$ of ∼500–800 mT (constituting 2–10 per cent of the SIRM for both the Garencuo and Wenbudangsang formations) or ∼2400 mT (constituting 18 per cent of the SIRM for the Garencuo Formation).

The test results of Lowrie (1990; Figs 5i–l) show that the soft (0.12 T) and most of the medium (0.4 T; Figs 5j–l) components were unblocked at ∼500–580 °C, indicating that component 1 is fine-grained magnetite (possibly with minor Fe-substitution). The medium and hard (2.4 T) components show slight inflections at ∼100–150 °C and ∼300–350 °C, suggesting the presence of goethite and the possible occurrence of pyrrhotite. When the temperature reached 680 °C, the medium (Fig. 5i) and hard (Figs 5i–l) components decreased to zero, indicating the presence of hematite. The hard components 2 and 3 with $B_{1/2}$ of ∼2000–2400 mT are interpreted by the presence of goethite, with $B_{1/2}$ of ∼250–800 mT are interpreted by the existence of pyrrhotite and/or hematite.

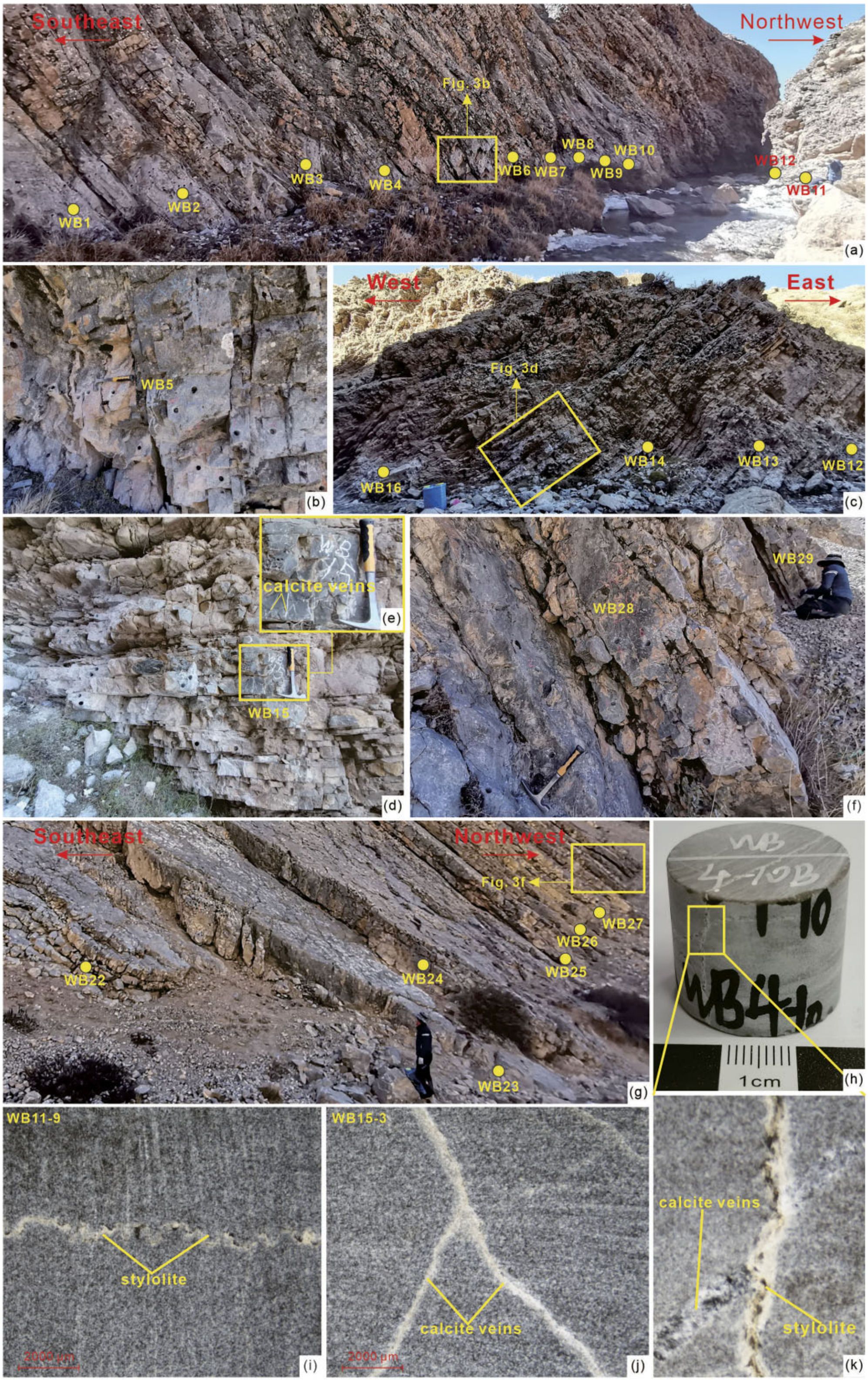

Figure 3. Photographs showing field outcrops, calcite veins, and stylolite from the Garencuo and Wenbudangsang formation limestones in the Wenbudangsang area. (a)–(e) Field outcrops of the Garencuo Formation. (f) and (g) Field outcrops of the Wenbudangsang Formation. (e) Calcite veins in the field outcrops. (h) and (k) Macroscopic calcite veins and stylolites on the surface of a sample. (i) and (j) Micrographic observations of stylolites and calcite veins.

The *k–T* curves are shown in Fig. S2. The heating curves are characterized by an increase in magnetic susceptibility between ∼380 and ∼500 °C (Figs S2a, c and d) or between ∼480 and ∼530 °C (Fig. S2b). These, together with the cooling curves, are higher than the heating curves below ∼400 °C, suggesting the transformation of iron-containing minerals to magnetite during heating. The heating curves show a significant drop at ∼580 °C, indicating the presence of magnetite.

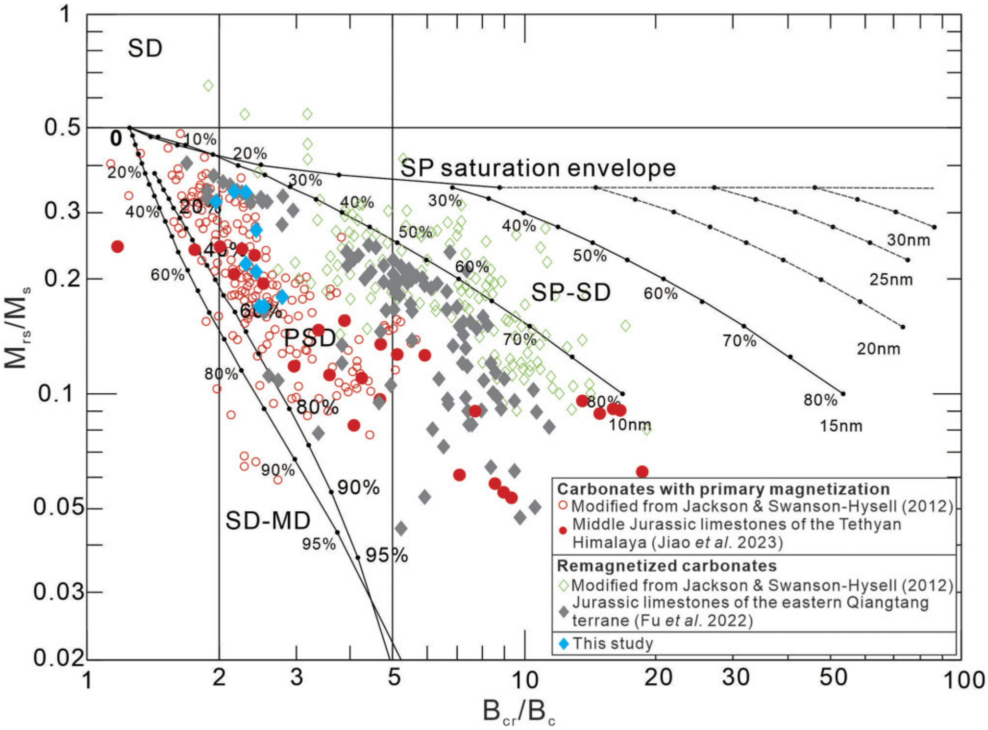

Figure 4. Day plot (Day *et al.* 1977; Dunlop 2002) of the hysteresis parameters of nine limestone samples from the Garencuo and Wenbudangsang formations and the remagnetized and non-remagnetized carbonate rocks reported by Jackson & Swanson-Hysell (2012), Fu *et al.* (2022) and Jiao *et al.* (2023).

4 PETROGRAPHY

Small calcite veins and stylolites are visible in some samples even though the samples were not taken near cracks or veins (Figs 3e and h–k). To better understand the microtextures and the composition of the iron oxides, polished thin sections of representative specimens were made for scanning electron microscopy (SEM) observations and energy dispersive spectrometry (EDS) analyses. These experiments were performed at the Electron Microprobe Analysis and Scanning Electron Microscope Laboratory at IGGCAS.

The SEM images and EDS analyses show that the Wenbudangsang and Garencuo formation limestones contain abundant iron oxides (Figs 6 and S3), usually distributed in the carbonates (Figs 6a, c and f), cracks (Figs 6a and d), or around the calcite veins (Fig. 6g). These iron oxides are characterized by framboids (Figs 6h and i) and irregular shapes (Figs 6a–c and f) with a size range from hundreds of nanometers to tens of microns. Some grains lack obvious oxidized rims (Fig. 6a), whereas other grains have obvious oxidized rims (Fig. 6f). These characteristics indicate that these framboidal oxides were formerly sulphides (mostly pyrite); therefore, most of the iron oxides observed in the limestones were authigenic.

5 PALAEOMAGNETISM

The remanent magnetization was measured using a 2 G 755–4 K cryogenic magnetometer housed in a magnetically shielded room (<300 nT). Demagnetization was performed using an ASC-TD 48 furnace, a Magnetic Measurements Thermal Demagnetizer Super Cooling, or an ASC Scientific D-2000 alternating field (AF) demagnetizer. To isolate the characteristic remanent magnetization (ChRM) directions, both thermal and AF demagnetizations were performed. Thermal demagnetization intervals were set to 80–40 °C below 280 °C and changed to 30–10 °C above 280 °C. The AF demagnetization steps were set to 2.5–5 mT below 20 mT and shifted to 10–20 mT above 20 mT. All the experiments were completed at PMEML at the China University of Geosciences, Beijing. The ChRM directions of all the specimens were determined using a principal component analysis (Kirschvink 1980) with at least four successive steps (anchored to the origin), and the site-mean directions were calculated using Fisherian statistics (Fisher 1953). Specimens with maximum angular deviations greater than 15° were discarded and omitted from further analysis. The software packages developed by Enkin (1990) and Cogné (2003) were used to analyse the palaeomagnetic data.

For the Lower Triassic Garencuo Formation, 121 specimens were subjected to stepwise thermal demagnetization and 79 specimens were treated with stepwise AF demagnetization. Representative Zijderveld diagrams (Zijderveld 1967) are shown in Fig. 7. Thermal and AF demagnetization of specimens from the same sampling site show similar demagnetization features (Figs 7j and k). Two magnetic components can be isolated from most specimens. The low-temperature (field) components can be isolated below 280 °C or 20 mT. The mean direction of this component in geographical coordinates is $D_g = 359.9°$, $I_g = 51.2°$, $k_g = 32.3$ and $\alpha_{95} = 1.9°$ ($n = 173$; Fig. S4a). This direction is close to the present geomagnetic field direction ($D = 1.3°$, $I = 50.7°$) and is interpreted as a component from a recent viscous remanent magnetization. After removing the soft components, a stable high-temperature (field) component decaying towards the origin can be determined between 280 and 370–580 °C or between 20 and 80–140 mT; this defines the ChRM. The site-mean ChRM direction (overall mean A) of the 21 sites is $D_g = 34.6°$, $I_g = 49.3°$, $k_g = 43.5$ and $\alpha_{95} = 4.9°$ *in situ* and $D_s = 345.5°$, $I_s = 33.3°$, $k_s = 39.2$ and $\alpha_{95} = 5.1°$ after tilt-correction (Fig. 8a, Tables 1 and S2).

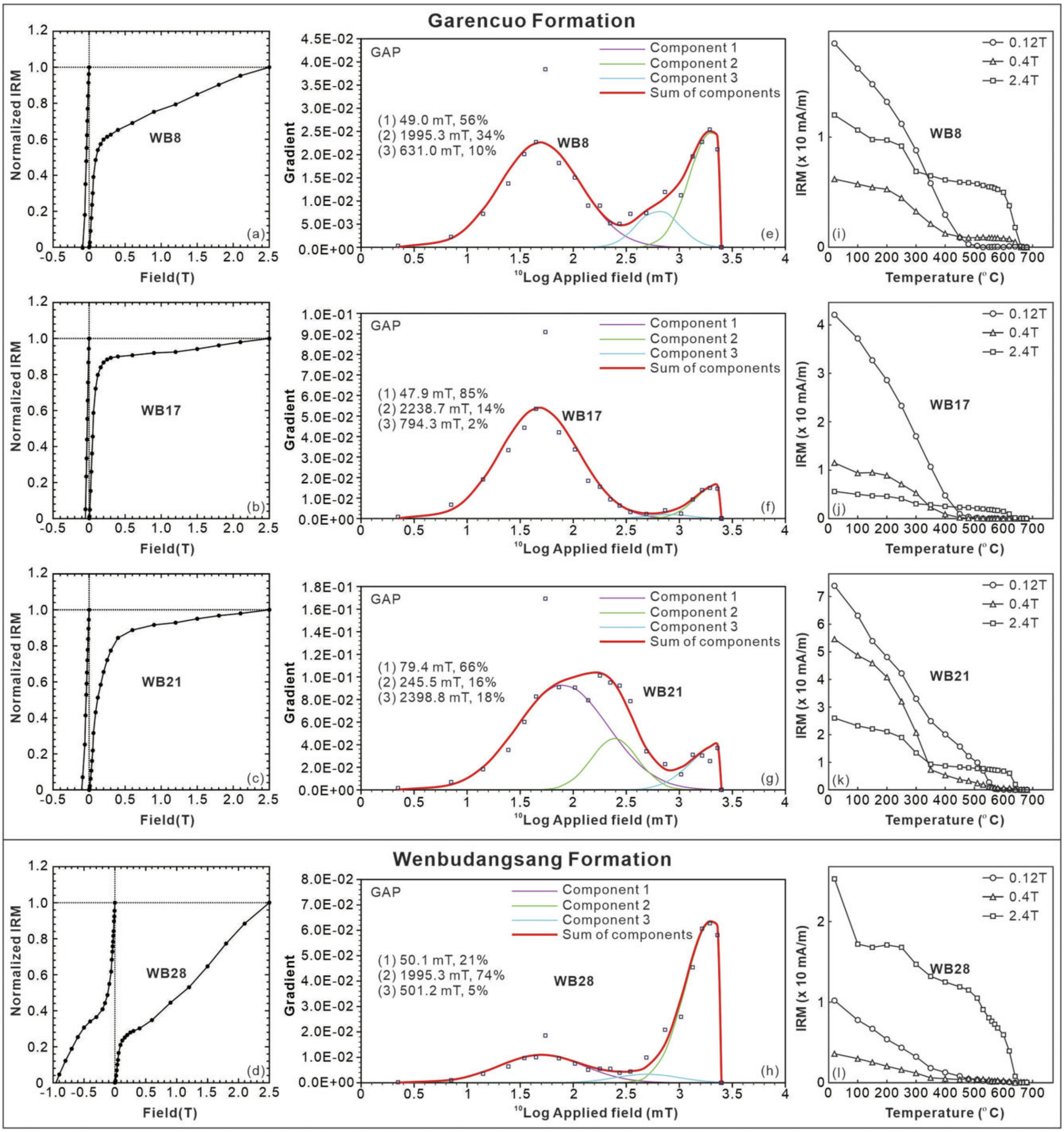

Figure 5. Rock magnetic experiments for representative samples. (a)–(d) IRM acquisition curves and back-field demagnetization of the SIRM curves. (e)–(h) Component analysis of the coercivity distributions (Kruiver *et al.* 2001). (i)–(l) Thermal demagnetization of the three-axis IRM curves of the representative samples. GAP indicates gradient acquisition plot.

For the Upper Permian Wenbudangsang Formation, 38 specimens were treated with stepwise thermal demagnetization and 30 specimens were subjected to stepwise AF demagnetization. Representative Zijderveld diagrams (Zijderveld 1967) are shown in Figs 7(q)–(t). No significant difference in the remanence direction was observed between the thermal and AF demagnetizations (Figs 7s and t). Similarly, most specimens yielded two magnetic components. The low-temperature (field) component was isolated below 280 °C or 20 mT. The mean direction of this component in geographical coordinates is $D_g = 352.8°$, $I_g = 51.3°$, $k_g = 28.2$ and $\alpha_{95} = 4.4°$ ($n = 38$; Fig. S4b). This direction is clustered around the present geomagnetic field direction ($D = 1.3°$, $I = 50.7°$), representing a recent viscous remanent magnetization. The high-temperature (field) component was isolated between 280 and 390–510 °C or between 20 and 70–120 mT. Notably, a small number of specimens showed erratic demagnetization patterns and a reliable ChRM direction could not be isolated from these specimens. Seven of eight sites provided the site-mean ChRM direction (overall mean B) of $D_g = 24.2°$, $I_g = 52.8°$, $k_g = 98.7$ and $\alpha_{95} = 6.1°$ *in situ* and $D_s = 335.6°$, $I_s = 30.7°$, $k_s = 111.2$

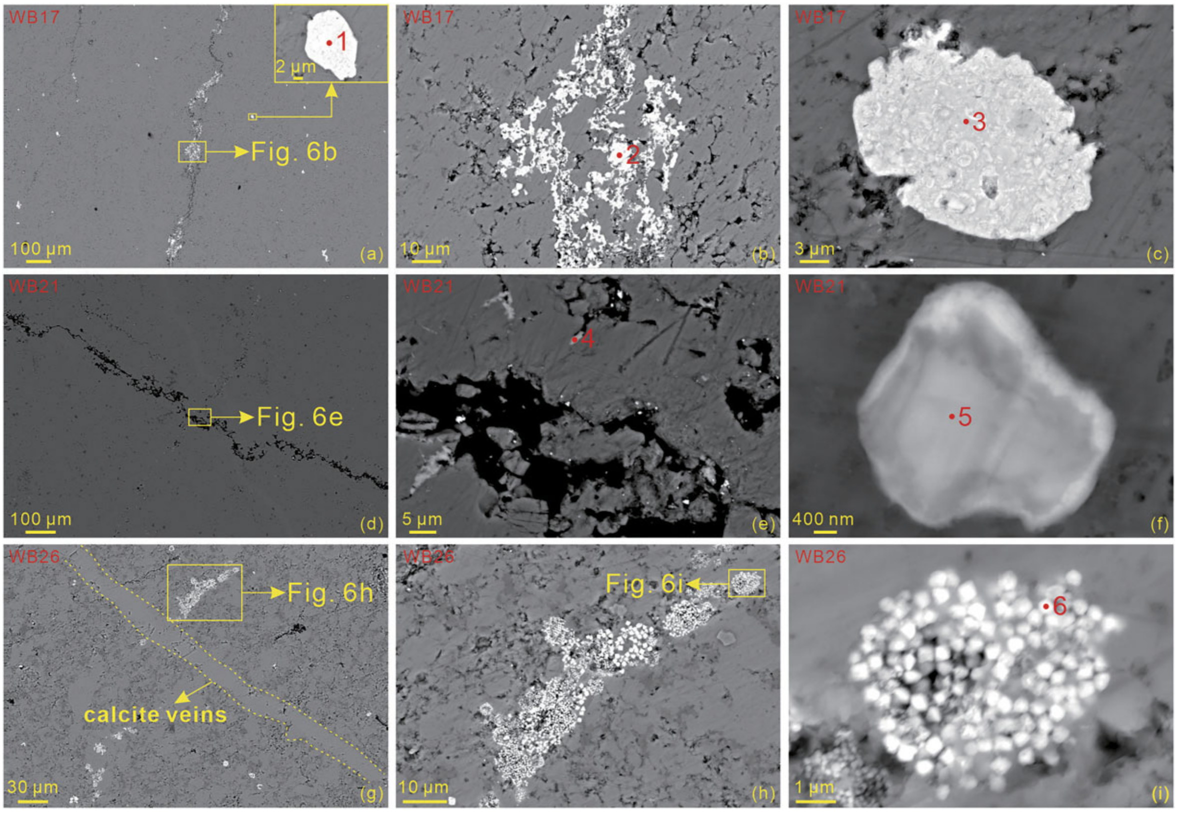

Figure 6. SEM observations. The red spots show the points analysed using EDS.

and α_{95} = 5.7° after tilt-correction (Fig. 8b, Tables 1 and S2).

Significantly, the site-mean ChRM direction of the Garencuo Formation limestone is generally consistent with that of the Wenbudangsang Formation limestone. Therefore, their ChRM directions can be averaged together. The site-mean ChRM direction (overall mean C) for the 28 sites is D_g = 32.1°, I_g = 50.3°, k_g = 47.9 and α_{95} = 4.0° *in situ* and D_s = 342.9°, I_s = 32.7°, k_s = 43.2 and α_{95} = 4.2° after tilt-correction (Fig. 8c). A mean palaeopole at 68.9°N, 314.4°E with A_{95} = 4.3° was obtained by averaging all of the site-level virtual geomagnetic poles (Table 1). The fold tests are not significant because the sampling section shows monoclinic features with minor variations in the bedding attitudes.

6 DISCUSSION

6.1 Timing of the remagnetization

Based on the conodont biostratigraphy (Wu *et al.* 2014), the Wenbudangsang and Garencuo formation limestones were dated to the Wuchiapingian through the Induan (∼259–251 Ma). This interval includes both reversed and normal polarities (Zhang *et al.* 2021). However, the ChRM directions from the Wenbudangsang and Garencuo formation limestones are all normal polarity, indicating that the primary remanence of the rocks was most likely overprinted. This is consistent with the SEM observations and EDS analyses, as mentioned above.

To constrain the timing of the remagnetization, we compared the palaeopole obtained in this study with those from the Lhasa terrane. The published Late Permian–Palaeogene palaeomagnetic datasets from the Lhasa terrane are summarized in Table 2 and are appraised using the newly updated R criteria (Meert *et al.* 2020). The palaeomagnetic datasets with *R*-value ≥6, in line with R4 (field tests that constrain the age of magnetization) or R6 (the presence of magnetic reversals) besides all five other R criteria, were used for further analyses. A total of 2 Triassic, 5 Jurassic, 32 Cretaceous and 14 Palaeogene palaeopoles satisfied our selection criteria (Table 2). Other palaeomagnetic datasets were not used because they lacked robust field tests, came from inadequate numbers of sites (less than eight sites) or samples (less than 25 samples), and/or resembled palaeopoles with younger ages (Table 2).

Because the fold tests were not significant, we first compared the palaeopole (62.8°N, 166.9°E, d*p*/d*m* = 3.6°/5.4°) calculated from the directions prior to tilt-correction with Late Permian–Palaeogene palaeopoles derived from the Lhasa terrane to constrain the timing of the remagnetization. As shown in Fig. 9 and Table 2, the palaeopole for the directions prior to tilt-correction (pink circles) in this study is comparatively distant from the Late Permian–Palaeogene palaeopoles obtained from the Lhasa terrane. In addition, we determined the palaeolatitude (31.1° ± 3.6°N) using the directions prior to tilt-correction. This palaeolatitude is commensurate with both the current latitude (32.3°N) and the Late Oligocene–Early Miocene (∼26–22 Ma) palaeolatitude (33.3° ± 2.6°N) of the Nima basin of the Lhasa terrane (Meng *et al.* 2017). The possibility of remagnetization during the Late Oligocene–Early Miocene is low because: (1) there was no Late Oligocene–Early Miocene magmatism near the study area (Fig. 2a); (2) the convergence within the Tibetan Plateau was significantly reduced around 26 Ma (Meng *et al.* 2017) and (3) the Tibetan Plateau region has not experienced any major events (such as continental collision) during the Late Oligocene–Early Miocene. Therefore, the remanence acquisition

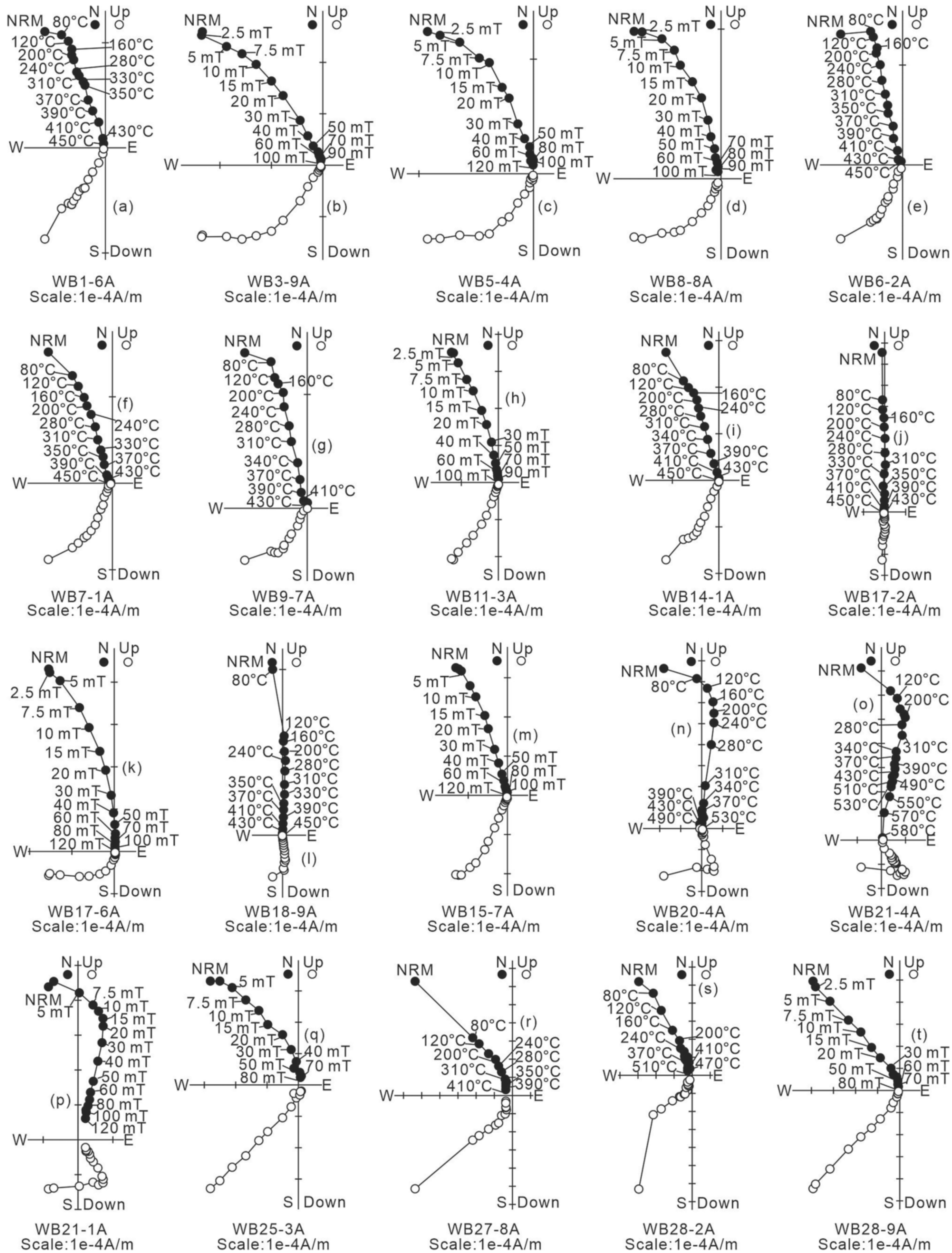

Figure 7. Zijderveld diagrams of representative specimens from the Upper Permian–Lower Triassic limestones in the Wenbudangsang area. Directions are plotted after bedding tilt-correction. The solid (open) symbols represent projections onto the horizontal (vertical) plane. NRM indicates natural remanent magnetization.

of the Wenbudangsang and Garencuo formation limestones likely occurred prior to tilting.

We compared the palaeopole (68.9°N, 314.4°E with $A_{95} = 4.3°$) calculated from the site-mean directions after tilt-correction with the Late Permian–Palaeogene palaeopoles obtained from the Lhasa terrane to constrain the timing of the remagnetization. As shown in Fig. 9 and Table 2, the palaeopole (blue circles) in this study is close to the Middle Jurassic palaeopole (ID 12, 66.8°N, 294.1°E

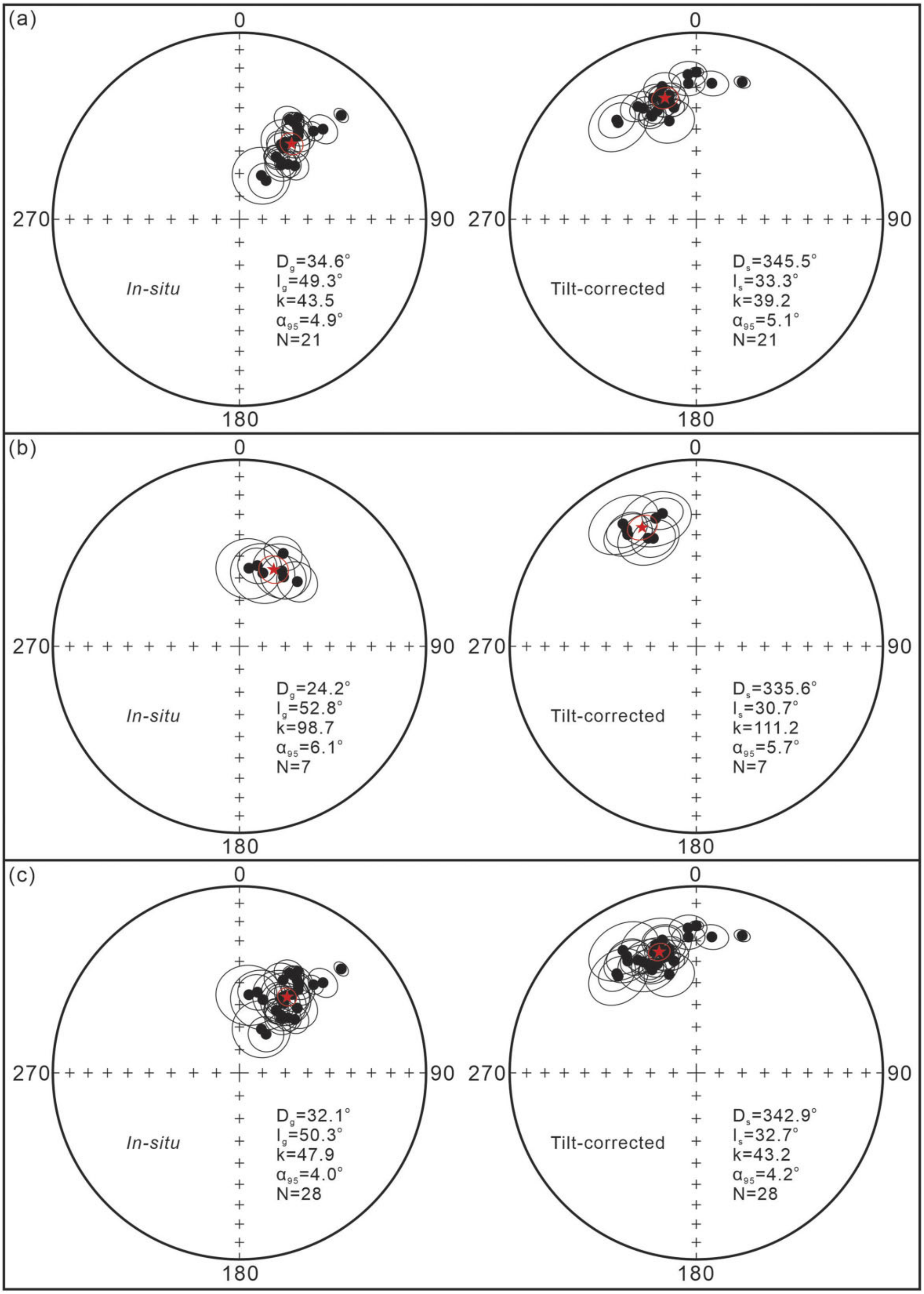

Figure 8. Equal-area projections of the site-mean ChRM directions from the Lower Triassic Garencuo Formation and Upper Permian Wenbudangsang Formation limestones before and after tilt-correction. (a) Garencuo Formation; (b) Wenbudangsang Formation and (c) Garencuo + Wenbudangsang formations. The stars indicate the overall mean directions.

with $dp/dm = 7.4°/14.5°$, Otofuji *et al.* 2007), the Early Cretaceous palaeopole (ID 22, 69.1°N, 319.8°E with $A_{95} = 4.8°$, Bian *et al.* 2017), the Late Cretaceous palaeopoles (ID 39, 67.1°N, 325.1°E with $A_{95} = 6.8°$, Yi *et al.* 2023; ID 40, 68.4°N, 298.8°E with $A_{95} = 2.7°$, Yi *et al.* 2015; ID 50, 70.2°N, 300.5°E with $dp/dm = 1.4°/2.7°$, Tan *et al.* 2010) and the Palaeocene palaeopoles (ID 56, 78.0°N, 329.0°E with $A_{95} = 5.9°$, Meng *et al.* 2012; ID 57, 71.6°N, 340.0°E with $A_{95} = 5.0°$, Li *et al.* 2022c; ID 58,

Table 1 Site-mean ChRM directions of the Wenbudangsang and Garencuo formation limestones from the Wenbudangsang area in the western Lhasa terrane.

Site	Strike/dip (°)	n/N	D_g (°)	I_g (°)	D_s (°)	I_s (°)	k	α_{95} (°)	Plat (°)	Plon (°)
WB1	207/58	9/10	37.5	60.0	332.6	32.4	55.2	7.0	61.3	328.9
WB2	207/58	10/10	34.5	69.5	321.3	32.4	40.5	7.7	52.2	339.6
WB3	205/54	10/10	26.6	68.6	321.0	33.8	15.9	12.5	52.4	341.1
WB4	208/55	9/9	46.0	56.1	340.3	38.1	72.6	6.1	69.4	326.0
WB5	205/52	9/9	41.4	57.7	336.8	39.7	82.1	5.7	67.3	333.4
WB6	205/52	10/10	30.8	58.2	334.4	34.4	79.7	5.4	63.4	329.0
WB7	204/46	9/10	30.4	58.1	336.6	39.2	112.2	4.9	66.9	332.9
WB8	213/54	7/9	36.0	58.8	340.5	31.7	81.1	6.7	66.8	317.0
WB9	213/54	8/8	31.9	53.1	345.6	27.4	63.0	7.0	67.9	302.8
WB10	207/49	8/8	29.1	52.1	343.6	32.3	83.1	6.1	69.1	312.0
WB11	194/57	9/9	40.0	38.3	348.7	38.8	152.4	4.2	75.6	309.8
WB12	194/57	10/10	28.8	40.0	343.8	30.9	129.3	4.3	68.6	310.0
WB13	193/54	9/10	31.9	41.1	344.5	35.7	67.8	6.3	71.3	314.7
WB14	195/49	9/9	26.5	40.0	347.8	32.5	72.7	6.1	71.7	302.9
WB15	195/40	10/10	30.8	50.2	344.6	44.5	23.3	10.2	75.2	332.4
WB16	203/49	10/10	34.0	48.0	347.0	35.7	42.2	7.5	72.9	309.0
WB17	216/55	9/9	35.2	44.6	356.7	23.3	57.0	6.9	69.6	272.3
WB18	211/50	9/10	34.0	43.0	356.7	27.9	69.4	6.2	72.3	273.5
WB19	211/50	10/10	29.8	37.5	360.0	22.2	359.3	2.6	69.2	263.0
WB20	211/55	8/9	42.8	34.5	6.5	27.5	78.8	6.3	71.3	243.0
WB21	211/55	11/11	44.4	23.1	18.5	23.5	226.5	3.0	63.7	218.5
Overall mean A			34.6	49.3	345.5	33.3	39.2	5.1	70.7	310.2
$N = 21$ sites									$K = 36.3$	$A_{95} = 5.4$
WB22	213/49				No reliable site-mean direction					
WB23	215/44	5/10	17.7	56.1	342.4	28.8	32.9	13.5	66.7	310.5
WB24	202/50	8/10	7.9	55.3	329.5	25.0	18.6	13.2	56.2	325.6
WB25	202/52	5/7	25.2	44.2	345.7	27.4	96.3	7.8	68.0	302.6
WB26	197/51	5/8	12.5	53.5	329.2	28.0	90.8	8.1	57.0	328.4
WB27	197/51	5/9	29.4	51.7	336.0	36.7	39.9	12.3	65.5	329.9
WB28	201/57	7/7	41.8	51.6	338.3	37.7	48.4	8.8	67.7	328.3
WB29	197/63	6/6	32.4	53.7	328.5	30.4	48.6	9.7	57.3	331.3
Overall mean B			24.2	52.8	335.6	30.7	111.2	5.7	63.0	323.4
$N = 7$ sites									$K = 123.5$	$A_{95} = 5.5$
Overall mean C			32.1	50.3	342.9	32.7	43.2	4.2	68.9	314.4
$N = 28$ sites									$K = 40.4$	$A_{95} = 4.3$

Note: Strike/dip, right hand strike/dip of the beds; n/N, number of samples used to calculate the site mean and those measured; $D_g/I_g(D_s/I_s)$, declination and inclination in geographic (stratigraphic) coordinates; k (K), the best estimate of the precision parameter; α_{95} (A_{95}), the radius that the mean direction (pole) lies within the 95 per cent confidence level and Plat/Plon, latitude and longitude of pole. The overall mean A, B and C represent the site-mean ChRM directions of the Garencuo, Wenbudangsang and Garencuo + Wenbudangsang formation limestones, respectively.

71.5°N, 300.1°E with $dp/dm = 6.4°/11.9°$, Achache *et al.* 1984; ID 69, 71.7°N, 339.3°E with $A_{95} = 3.1°$, Ding *et al.* 2015) at the 95 per cent confidence level. This result suggests that there may have been a remagnetization of the limestones during the Middle Jurassic–Palaeocene. Considering that our samples were collected from the western Lhasa terrane and that palaeopoles are influenced by vertical axis rotations, we prefer to compare the newly obtained palaeopole with Late Permian–Palaeogene palaeopoles from the western Lhasa terrane (west of 87°E) to constrain the timing of the remagnetization. As shown in Fig. 9, the palaeopole (blue circles) in this study is close to the Early Cretaceous (ID 22, Bian *et al.* 2017), Late Cretaceous (ID 40, Yi *et al.* 2015) and Palaeocene (ID 56, Meng *et al.* 2012; ID 57, Li *et al.* 2022c; ID 69, Ding *et al.* 2015) palaeopoles at the 95 per cent confidence level. Considering that (1) the ChRM directions of the Wenbudangsang and Garencuo formation limestones were likely acquired prior to tilting and (2) the unconformity between the Upper Permian–Lower Triassic strata and the Lower Cretaceous strata indicates that the tilting time in the studied area likely occurred prior to or during the Early Cretaceous, the limestones were likely remagnetized during the Early Cretaceous.

6.2 Mechanisms for the remagnetization and their tectonic implications

Two widely accepted explanations for the phenomenon of remagnetization are: thermoviscous resetting of existing magnetic minerals (Kent 1985; Harlan *et al.* 1996), and chemical remanent magnetization (CRM) via the growth of magnetic minerals related to tectonic fluid migration (Katz *et al.* 2000; Van der Voo & Torsvik 2012; Huang *et al.* 2015; Fu *et al.* 2022). The strata of the Wenbudangsang and Garencuo formations can be correlated with the Mujiucuo Formation in the Cuoqin Basin (Ji *et al.* 2018). The homogenization temperatures of the brine inclusions in the Mujiucuo Formation dolomite tend to range from 120 to 180 °C (Zhang 2016), indicating that the Mujiucuo Formation experienced moderate burial temperatures. Based on the relaxation time-blocking temperature relations for magnetite reported by Pullaiah *et al.* (1975) and Dunlop *et al.* (2000), the unblocking temperatures of the Upper Permian–Lower Triassic limestones in the study area are between 410 and 580 °C, resulting in burial temperatures of ∼200–560 and ∼180–550 °C, respectively. These rocks are not metamorphic and burial temperatures higher than 220–250 °C are unrealistic. The relatively low

Table 2 Summary of late permian–palaeogene palaeomagnetic results from the lhasa terrane.

ID	Lithology	Area	Slat (°N)	Slon (°E)	Age (Ma)	Plat (°N)	Plon (°E)	A_{95} (dp/dm) (°)	Palaeolat (°N)	n/N	Criterion (R)	References
1[a]	Lim	Cuoqin	30.8	84.9	P_3	52.3	256.3	14.9/7.6	−5.2 ± 7.6	17/2	1□3□5□7 (4)	Guo (2009)
2	Lim	Geji	32.3	83.0	P_3-T_1	68.9	314.4	4.3	18.0 ± 4.3	234/28	123□5□□ (4)	This study
3[a]	Dolomites	Xainza	31.0	89.0	P_3	68.5	228.5	12.6/22.3	14.0 ± 12.6	34/5	123□5□□ (4)	Ran *et al.* (2012)
4	Lim	Cuoqin	30.9	84.7	T_{1-2}	18.9	208.4	3.9	−16.9 ± 3.9	47/8	123F5R7 (7)	Zhou *et al.* (2016)
5[a]	Lim	Cuoqin	31.1	85.3	T	17.4	205.9	6.1	−16.2 ± 6.1	28/5	□23F5□7 (5)	Cheng *et al.* (2015)
6[a]	Silicalites	Xainza	31.0	89.0	T_3	50.5	221.3	2.9/5.7	0.6 ± 2.9	11/2	1□3□5□□ (3)	Ran *et al.* (2012)
7[a]	VR	Dazi	29.4	91.3	T_3	8.2	211.6	4.0/7.0	−26.5 ± 4.0	22/5	1□3□5□7 (4)	Dong *et al.* (1991)
8	Lim	Cuoqin	30.9	84.7	T_3	19.6	211.8	10.7	−18.6 ± 10.7	37/6	123F5□7 (6)	Zhou *et al.* (2016)
9	Volc	Sangri	29.3	92.0	∼180	51.7	305.8	1.7/3.4	2.0 ± 1.7	–/61	123□5R7 (6)	Li *et al.* (2016)
10	Volc	Xigaze	29.4	88.6	∼183–173	33.5	312.3	5.0	−9.5 ± 5.0	138/27	123F5R7 (7)	Ma *et al.* (2022b)
11	Volc	Lhasa	29.7	91.3	∼170	29.8	180.7	5.7	9.6 ± 5.7	124/21	123F5R7 (7)	Wang *et al.* (2023)
12	RB	Basu	30.1	96.9	J_2	66.8	294.1	7.4/14.5	11.9 ± 7.4	53/8	123F5R7 (7)	Otofuji *et al.* (2007)
13[a]	Sand	Dazi	29.4	91.3	J_{2-3}	51.0	293.1	5.3/10.4	−2.6 ± 5.3	13/4	1□□□5□7 (3)	Dong *et al.* (1991)
14[a]	VR	Daxiong	30.5	85.0	J	28.8	308.8	7.7/13.7	−15.0 ± 7.7	-/-	□□□□5□7 (2)	Ye *et al.* (1987)
15[a]	Greywacke	Sangxiong	31.1	91.5	J_3	50.2	290.1	4.0/7.8	−4.1 ± 4.0	32/6	12□□5□7 (4)	Dong *et al.* (1991)
16[a]	Lim	Lhasa	29.6	91.1	J_3	59.0	280.4	16.6	2.4 ± 16.6	21/-	1□□□5□7 (3)	Zhu *et al.* (1981)
17[a]	Sand	Gerze	32.0	84.0	J_3	-36.2	106.2	6.9/12.0	−18.1 ± 6.9	-/-	1□3□5□7 (4)	Ye *et al.* (1987)
18[a]	Lim	Lhasa	29.6	91.1	J_3	59.0	280.4	16.6	2.4 ± 16.6	21/-	1□□□5□7 (3)	Zhu *et al.* (1981)
19	Volc	Geji	32.0	82.0	∼157–153	45.3	295.3	2.5	−7.0 ± 2.5	325/46	123F5R7 (6)	Li *et al.* (2022b)
20[a]	Lim	Shiquanhe	32.7	80.2	K	67.7	234.2	13.1/24.5	12.3 ± 13.1	22/3	□□3□5□7 (3)	Chen *et al.* (1993)
21	Volc	Cuoqin	31.4	85.1	∼131–110	58.2	341.9	4.6	21.6 ± 4.6	162/18	123F5R7 (7)	Chen *et al.* (2012)
22	Volc + Lim	Shiquanhe	32.2	80.4	∼116–113	69.1	319.8	4.8	19.5 ± 4.8	205/19	123F5□7 (6)	Bian *et al.* (2017)
23	Volc	Yanhu	32.3	82.6	∼132–120	61.4	192.9	2.1	19.4 ± 2.1	444/51	123F5D7 (7)	Ma *et al.* (2014)
24	Volc	Cuoqin	31.1	84.4	∼121–117	70.5	292.9	7.4	15.0 ± 7.4	116/12	123F5D7 (7)	Yang *et al.* (2015a)
25	Volc + RB	Gerze	32.4	83.4	∼120–106	38.7	159.6	1.7/2.6	29.1 ± 1.7	198/24	123F5D7 (7)	Wang *et al.* (2022)
26	RB	Gerze	32.4	83.4	∼120–106	75.2	278.1	1.5/2.6	17.9 ± 1.5	255/32	123F5D7 (7)	Wang *et al.* (2022)
27	Volc	Luolong	30.7	95.9	∼125	60.9	227.2	2.4/4.6	7.7 ± 2.4	17/142	123F5R7 (7)	Cao *et al.* (2023)
28	Volc + Sand	Naqu	31.3	91.9	∼120.2	66.9	281.2	6.1	10.2 ± 6.1	139/19	123F5D7 (7)	Li *et al.* (2017a)
29[a]	Volc	Deqin	30.5	90.1	∼114	66.4	220.3	6.9	13.9 ± 6.9	88/15	123□5□7 (5)	Sun *et al.* (2008)
30	Volc	Naqu	31.5	92.1	∼114–110	72.0	252.6	6.7	14.6 ± 6.7	59/9	123F∗5R∗7 (7)	Li *et al.* (2022a)

Table 2 Continued

ID	Lithology	Area	Slat (°N)	Slon (°E)	Age (Ma)	Plat (°N)	Plon (°E)	A_{95} (d*p*/d*m*) (°)	Palaeolat (°N)	*n*/*N*	Criterion (R)	References
31	RB	Namuqie	31.6	91.4	~114–100	64.2	324.2	1.9	17.7 ± 1.9	480/50	123F5□7 (6)	Bian *et al.* (2023)
32	Lim	Shiquanhe	32.2	80.8	~113–72	68.0	211.1	1.9	17.5 ± 1.9	274/38	123F5R7 (7)	Ma *et al.* (2018)
33	Volc	Nima	31.7	87.5	105–100	42.2	355.9	7.5	23.0 ± 7.5	117/18	123F5□7 (6)	Niu *et al.* (2023)
34	Volc	Cuoqin	30.6	85.2	~99–93	63.1	224.6	5.1	10.2 ± 5.1	112/14	123F5□7 (6)	Tang *et al.* (2013)
35	Volc	Shiquanhe	32.4	80.1	~92.5	64.1	209.0	9.6	15.3 ± 9.6	78/10	123F5R7 (7)	Yi *et al.* (2015)
36[a]	Volc	Naqu	31.5	92.0	~96	78.0	282.0	4.0/6.9	20.9 ± 4.0	33/9	123□□□7 (4)	Lin & Watts (1988)
37	RB	Linzhou	29.9	91.2	~91–70	71.1	262.0	5.5	13.4 ± 5.5	206/27	123F5□7 (6)	Ma *et al.* (2022a)
38[a]	Volc	Chalicuo	31.7	91.0	~90	74.0	318.0	11.1/19.1	22.3 ± 11.1	20/4	1□3□□□□ (2)	Lin & Watts (1988)
39	Dyke	Lhasa	29.5	90.0	~83	67.1	325.1	6.8	19.8 ± 6.8	126/15	123□5D7 (7)	Yi *et al.* (2023)
40	Volc	Yare	31.6	82.2	~80	68.4	298.8	2.7	14.1 ± 2.7	136/15	123F5□7 (6)	Yi *et al.* (2015)
41	RB + Volc	Linzhou	29.9	91.1	75–68	70.5	269.6	4.9	12.9 ± 4.9	164/21	123□5R7 (6)	Cao *et al.* (2017b)
42	Volc + RB	Maxiang	29.9	90.7	~74.2–70.2	70.1	265.2	4.6	12.4 ± 4.6	433/36	123F5R7 (7)	Tong *et al.* (2022)
43	Lim + Sand	Zhongba	29.9	84.3	72–66	67.1	347.5	7.1	27.4 ± 7.1	42/-	123F5R7 (7)	Li *et al.* (2022c)
44	Volc	Shiquanhe	32.4	80.1	~68	47.8	181.4	6.4	18.2 ± 6.4	300/17	123F5D7 (7)	Ma *et al.* (2017)
45	RB	Geji	32.7	81.4	K_2	74.4	226.0	3.8	19.5 ± 3.8	431/54	123F5□7 (6)	Bian *et al.* (2020)
46	RB	Cuoqin	31.2	84.7	K_2	49.0	344.3	5.3	18.6 ± 5.3	291/33	123F5D7 (7)	Yang *et al.* (2015a)
47	Volc	Linzhou	29.9	91.2	K_2	69.1	191.7	3.3/5.4	23.7 ± 3.3	132/21	123F5□7 (6)	Tan *et al.* (2010)
48	RB + Volc	Maxiang	29.9	90.7	K_2	75.0	306.7	6.8	21.0 ± 6.8	126/20	123F5□7 (6)	Sun *et al.* (2010)
49	RB	Dingqing	31.1	95.6	K_2	71.4	273.1	5.2	13.9 ± 5.2	150/15	123F5□7 (6)	Tong *et al.* (2017)
50	RB	Linzhou	29.9	91.2	K_2	70.2	300.5	1.4/2.7	16.0 ± 1.4	377/43	123F5D7 (7)	Tan *et al.* (2010)
51	RB	Linzhou	29.9	91.2	K_2	68.0	340.0	6.7/11.6	25.1 ± 6.7	68/7	123F5D7 (7)	Pozzi *et al.* (1982)
52	RB	Barda	31.7	91.5	K_2	63.5	325.4	6.5	17.7 ± 6.5	49/6	123F5□7 (6)	Achache *et al.* (1984)
53	RB	Linzhou	29.9	91.1	K_2	71.2	288.4	7.9	15.1 ± 7.9	61/8	123F5□7 (6)	Achache *et al.* (1984)
54	RB	Nima	31.8	87.2	K_2	71.2	241.9	5.5/10.0	14.6 ± 5.5	59/8	123□5R7 (6)	Cao *et al.* (2017a)
55	RB	Nima + Bange	31.8	87.7	K_2	63.3	329.4	3.6	19.0 ± 3.6	224/22	123F5□7 (6)	Liu *et al.* (2022)
56	Sed	Zhongba	29.9	84.3	57–54	78.0	329.0	5.9	26.8 ± 5.9	62/–	123F5□7 (6)	Meng *et al.* (2012)
57	Lim + Sand	Zhongba	29.9	84.3	57–54	71.6	340.0	5.0	26.6 ± 5.0	87/–	123F5R7 (7)	Li *et al.* (2022c)
58	Volc	Linzhou	29.9	91.1	~60–48	71.5	300.1	6.4/11.9	17.0 ± 6.4	46/8	123F5D7 (7)	Achache *et al.* (1984)
59	Tuff	Mendui	30.1	90.9	~55	73.6	274.3	7.3	16.2 ± 7.3	99/14	123F5D7 (7)	Sun *et al.* (2010)
60	Tuff	Linzhou	30.0	91.2	43–40	87.1	82.6	5.7	35.2 ± 5.7	76/9	123F5□7 (6)	Tan *et al.* (2010)

Table 2 Continued

ID	Lithology	Area	Slat (°N)	Slon (°E)	Age (Ma)	Plat (°N)	Plon (°E)	A_{95} (d*p*/d*m*) (°)	Palaeolat (°N)	*n*/*N*	Criterion (R)	References
61	Dyke	Linzhou	30.0	91.1	~53	68.9	225.4	5.8/10.6	14.9 ± 5.8	68/10	123F5D7 (7)	Liebke *et al.* (2010)
62	Volc	Linzhou	30.0	91.1	54–47	77.6	211.3	5.0	24.2 ± 5.0	195/24	123F5D7 (7)	Dupont-Nivert *et al.* (2010)
63	Volc	Linzhou	30.0	91.1	~64–60	66.4	262.5	6.3	8.7 ± 6.3	134/20	123F5D7 (7)	Chen *et al.* (2010, 2014)
64	Volc	Linzhou	30.0	91.1	~64–60	62.7	240.7	3.7/7.2	6.7 ± 3.7	78/13	123F5□□ (5)	Huang *et al.* (2015)
65	Volc	Linzhou	30.0	91.1	~64–60	65.8	254.1	4.4	8.3 ± 4.4	228/35	123C5D7 (7)	Yi *et al.* (2021)
66	Volc + Sed	Linzhou	30.0	91.1	~60–50	69.7	268.6	6.3	12.1 ± 6.3	90/13	123F5D7 (7)	Chen *et al.* (2010, 2014)
67	Volc	Linzhou	30.0	91.1	~50–44	69.1	234.2	5.6	13.6 ± 5.6	88/17	123F5D7 (7)	Chen *et al.* (2010, 2014)
68[a]	Volc + Sed	Linzhou	30.0	91.2	54–43	68.4	243.0	1.9	11.8 ± 1.9	119/–	123□5□7 (5)	Huang *et al.* (2013)
69	RB	Gerze	32.2	84.3	Oligocene	71.7	339.3	3.1	26.4 ± 3.1	471/35	123F5R7 (7)	Ding *et al.* (2015)
70	RB	Nima	31.8	87.2	~26–22	78.9	164.1	3.7/2.6	33.3 ± 2.6	233/–	123F5R7 (7)	Meng *et al.* (2017)

Note: ID, palaeopole abbreviations used in the plot; Sed, Sedimentary rocks; Lim, Limestones; Sand, Sandstones; Volc, Volcanic rocks; RB, Red beds; VR, Volcaniclastic rocks; Criteria (R), data quality criteria (number of criteria met) following Meert *et al.* (2020) (1, well-determined rock age and a presumption that magnetization is of the same age; 2, techniques and statistical analysis; 3, evaluation of remanence carriers; 4, field tests that constrain the age of magnetization; 5, structural control and tectonic coherence with the craton or block involved, inclination shallowing assessed in clastic sedimentary rocks; 6, the presence of reversals; 7, no resemblance to palaeopoles of younger ages [by more than a period]); F, positive fold test; F∗, positive fold test with additional data from the adjacent sampling area; R, positive reversal test; R∗, positive reversal test with additional data from the adjacent sampling area; D, dual-polarity and □, failed to meet the criterion; IDs with [a] are not used because these palaeomagnetic results did not meet our selection criteria.

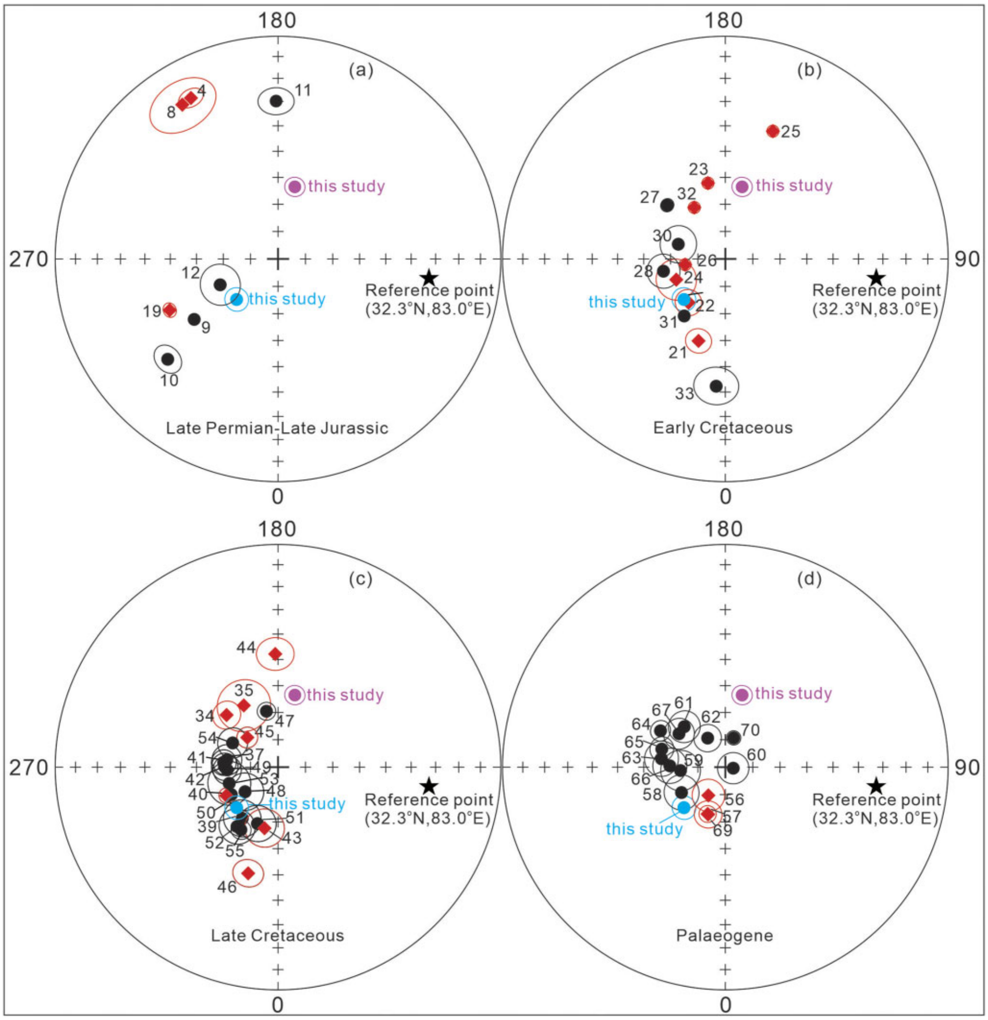

Figure 9. Equal-area projections showing the reliable Late Permian–Palaeogene palaeopoles obtained from the Lhasa terrane. (a) Late Permian–Late Jurassic palaeopoles; (b) Early Cretaceous palaeopoles; (c) Late Cretaceous palaeopoles and (d) Palaeogene palaeopoles. Black circles indicate the palaeopoles obtained from the central eastern Lhasa terrane. Red squares indicate the palaeopoles obtained from the western Lhasa terrane. The pink circles indicate the palaeopole calculated in this study from the directions prior to tilt-correction. The blue circles indicate the palaeopole calculated in this study from the site-mean directions after tilt-correction. The numbers on the panels refer to the studies listed in Table 2.

burial temperatures (<200 °C) indicate that the remagnetization of the Upper Permian–Lower Triassic limestones cannot be attributed to thermoviscous resetting.

Authigenic magnetite is widely present in remagnetized carbonates such as those found in the Tethyan Himalaya (Huang *et al.* 2015, 2017a, b; Dannemann *et al.* 2022), Lhasa terrane (Ran *et al.* 2012) and Qiangtang terrane (Huang *et al.* 2019; Fu *et al.* 2022; Yu *et al.* 2022). Authigenic magnetite can form from the oxidation of pyrite (or iron sulphides) under the influence of tectonic fluid migration (Suk *et al.* 1990; Huang *et al.* 2015; Fu *et al.* 2022). The palaeomagnetic and rock magnetic results indicate that the predominant magnetic carriers of the Upper Permian–Lower Triassic limestones are magnetite. The petrographic results indicate that some of the iron oxides were distributed in cracks or around the calcite veins and are characterized by framboids. These framboid-shaped iron oxides are interpreted as being magnetite pseudomorphs after pyrite. Therefore, we conclude that the main mechanism of remagnetization in the Upper Permian–Lower Triassic limestones was the oxidation of iron sulphides to magnetite. The existence of calcite veins and stylolites in some samples suggest that this mechanism was most likely related to tectonic fluid migration.

The sedimentary environment of the Upper Permian–Lower Triassic limestones and the redox circumstances at the time of their deposition likely facilitated the remagnetization. The Wenbudangsang and Garencuo formation limestones were deposited in a marine carbonate slope depositional environment (Ji *et al.* 2007; Wu *et al.* 2014, 2018). This indicates that the limestones were deposited in a shallow water environment. Furthermore, conodonts (especially hindeodids) discovered at the base of the Garencuo Formation indicate that they were well adapted to the shallower water environment (Wu *et al.* 2014). The abundant conodont fossils identified in the limestones suggest that the organic carbon contents were high. Following post-depositional degradation of sedimentary organic matter, microorganisms sequentially consume oxygen, nitrate, manganese oxides, iron oxides and sulphate until either all oxidants are consumed or all of the reactive organic matter is depleted (Froelich *et al.* 1979; Roberts *et al.* 2013). In this case, a sulphidic diagenesis environment would arise and the primary magnetization would be erased or overprinted during burial and diagenesis (Roberts 2015; Huang *et al.* 2019). Notably, the Risong Formation strata (∼40 km northeast of the studied area) were deposited during the Early Cretaceous (∼120–106 Ma) based on U-Pb dating of the interbedded volcanic rocks and sandstones (Wang *et al.* 2022). The age of the Risong Formation strata is broadly similar to that of the Duoni Formation strata (∼123–115 Ma; Sun *et al.* 2017) of the Cuoqin Basin. According to sedimentological studies in the Cuoqin Basin, continental fluvial environments formed during the Duoni Formation deposition, whereas some volcanic-influenced highlands formed during the eruption of the Zenong Group volcanic rocks (Sun *et al.* 2017). Therefore, we believe that, during the Early Cretaceous, the environment of the Upper Permian–Lower Triassic limestones may have changed from anoxic to suboxic and oxic, leading to the oxidation of iron sulphide to authigenic magnetite and the acquisition of CRM.

Although remagnetization can occur during any period in geological history, it is often associated with certain tectonic events. The collision of the Lhasa and Qiangtang terranes is critical in the formation of the Tibetan Plateau (Kapp *et al.* 2003; Ma *et al.* 2018; Hu *et al.* 2022). Because our data came from the western Lhasa terrane and the Lhasa–Qiangtang collision may have been diachronous (Yan *et al.* 2016; Wang *et al.* 2023), we only considered the western section of this collision zone (west of 87°E). For the western part of the Lhasa and Qiangtang terranes, numerous pieces of geological evidence point towards a collision time between the Late Jurassic and the Early Cretaceous. Such evidence includes the following: (1) structural mapping and U-Pb detrital zircon dating of the Domar fold-thrust belt in the western Qiangtang terrane show that the initial Lhasa-Qiangtang collision occurred from the Late Jurassic–Early Cretaceous (Raterman *et al.* 2014); (2) petrographic, U-Pb detrital zircon dating, and Lu-Hf isotopic data from the Wuga and Jingzhushan formations in the Gaize area of the western Lhasa terrane reveal that the initial Lhasa-Qiangtang collision most likely occurred during the latest Jurassic (∼150 Ma; Li *et al.* 2017b) and (3) mapping and geochronologic studies of the Shiquanhe area in the western Lhasa terrane suggest that the Lhasa-Qiangtang collision occurred between the Late Jurassic and the Early Cretaceous (Kapp *et al.* 2003). Following the Lhasa-Qiangtang collision, the Wenbudangsang area experienced convergence throughout the Late Jurassic and the Early Cretaceous. This process could have resulted in tectonic fluid migration and the formation of calcite veins and stylolites in the Upper Permian–Lower Triassic limestones, resulting in the CRM of the limestones.

6 CONCLUSIONS

We presented rock magnetic, petrographic and palaeomagnetic results from the Upper Permian–Lower Triassic limestones in the western Lhasa terrane. These results, along with reliable Late Permian–Palaeogene palaeomagnetic data from the Lhasa terrane and numerous pieces of geological evidence from the western part of the Lhasa and Qiangtang terranes, led us to draw the following conclusions:

(1) The Upper Permian–Lower Triassic limestones provide an Early Cretaceous remagnetized palaeopole located at 68.9°N, 314.4°E with $A_{95} = 4.3°$, corresponding to a palaeolatitude of 18.0° ± 4.3°N.

(2) CRM caused by the growth of magnetic minerals related to tectonic fluid migration was most likely the mechanism for limestone remagnetization.

(3) Tectonic fluid migration and the formation of calcite veins and stylolites in the limestones may have occurred during the Late Jurassic–Early Cretaceous convergence of the western Lhasa and Qiangtang terranes.

SUPPORTING INFORMATION

Supplementary data are available at *GJI* online.

Figure S1. Hysteresis loops after high-field slope correction for representative samples.

Figure S2. Temperature dependence of magnetic susceptibility (*k*–*T* curves) for representative samples.

Figure S3. EDS analyses corresponding to the points indicated in Fig. 6.

Figure S4. Equal-area projections of the specimen-mean directions of the low-temperature component (LTC).

Table S1. Hysteresis parameter for individual specimens at room temperature.

Table S2. Characteristic remanent magnetization (ChRM) directions for the Upper Permian–Lower Triassic limestones in the western Lhasa terrane.

Please note: Oxford University Press is not responsible for the content or functionality of any supporting materials supplied by the authors. Any queries (other than missing material) should be directed to the corresponding author for the paper.

ACKNOWLEDGMENTS

We sincerely thank Editor Andy Biggin, Professor Mark J. Dekkers and another anonymous reviewer for their constructive comments and suggestions that greatly improved this paper. This research was supported by the National Natural Science Foundation of China (41888101, 42004050, 42072257 and 41630104), the Fundamental Research Funds for the Central Universities (2652022001) and the Chinese '111' Project (B20011).

DATA AVAILABILITY

The data underlying this paper are available in the Supporting Information, and also available for download at https://doi.org/10.6084/m9.figshare.25122731.

REFERENCES

Achache, J., Courtillot, V. & Zhou, Y.X., 1984. Paleogeographic and tectonic evolution of southern Tibet since middle Cretaceous time: new paleomagnetic data and synthesis. *J. geophys. Res.,* **89,** 10 311–10 339.

Appel, E., Crouzet, C. & Schill, E., 2012. Pyrrhotite remagnetizations in the Himalaya: a review. *Geol. Soc (Lond.) Spec. Publ.,* **371,** 163–180.

Appel, E., Li, H., Patzelt, A. & Wang, J., 1998. Palaeomagnetic results from late Cretaceous and early tertiary limestones from the Tingri area in southern Tibet, China. *J. Nepal Geol. Soc.,* **18,** 113–124.

Bian, W.W. *et al.*, 2019. Paleomagnetic and geochronological results from the Zhela and Weimei Formations lava flows of the eastern Tethyan Himalaya: new insights into the breakup of eastern Gondwana. *J. geophys. Res.,* **124,** 44–64.

Bian, W.W. *et al.*, 2020. Paleomagnetism of the late Cretaceous red beds from the far western Lhasa Terrane: inclination discrepancy and tectonic implications. *Tectonics,* **39,** e2020TC006280

Bian, W.W. *et al.*, 2021. Paleomagnetic constraints on the India-Asia collision and the size of Greater India. *J. geophys. Res.,* **126,** e2021JB021965.

Bian, W.W. *et al.*, 2023. Location and shape of the Lhasa terrane prior to India-Asia collision. *Geol. Soc. Am. Bull.,* **588,** 110821. doi: 10.1130/B36647.1.

Bian, W.W., Yang, T.S., Ma, Y.M., Jin, J.J., Gao, F., Zhang, S.H., Wu, H.C. & Li, H.Y., 2017. New early Cretaceous paleomagnetic and geochronological results from the far western Lhasa terrane: contributions to the Lhasa-Qiangtang collision. *Sci. Rep.,* **7,** 16216.

Cao, Y. *et al.*, 2017b. New late Cretaceous paleomagnetic data from volcanic rocks and red beds from the Lhasa terrane and its implications for the paleolatitude of the southern margin of Asia prior to the collision with India. *Gondwana Res.,* **41,** 337–351.

Cao, Y. *et al.*, 2020. Paleomagnetism and U-Pb geochronology of early Cretaceous volcanic rocks from the Qiangtang Block, Tibetan Plateau: implications for the Qiangtang-Lhasa collision. *Tectonophysics,* **789,** doi:10.1016/j.tecto.2020.228500.

Cao, Y. *et al.* 2023. Paleomagnetism and geochronology of early Cretaceous volcanic rocks in the eastern segment of the Lhasa terrane, Tibetan Plateau, and their tectonic implications. *Geol. Soc. Am. Bull.,***135**(11-12), 3228–3240.

Cao, Y., Sun, Z.M., Li, H.B., Ye, X.Z., Pan, J.W., Zhang, L., Liu, D.L. & Liu, C.G., 2019. Paleomagnetic study of the late Triassic limestones in the western portion of the Qiangtang Block and its tectonic implications. *Acta Geol. Sin.,* **93,** 2463–2476. (in Chinese).

Cao, Y., Sun, Z.M., Liu, D.L., Zhang, L., Ye, X.Z., Zheng, Y. & He, X.L., 2017a. Late cretaceous paleomagnetic results in the Nyima area from the northern margin of the Lhasa block and its tectonic implications. *Acta Petrol. Sin.,* **33**(12), 3989–3998. (in Chinese).

Channell, J.E.T. & McCabe, C., 1994. Comparison of magnetic hysteresis parameters of unremagnetized and remagnetized limestones. *J. geophys. Res.,* **99,** 4613–4623.

Chatterjee, S., Goswami, A. & Scotese, C.R., 2013. The longest voyage: tectonic, magmatic, and paleoclimatic evolution of the Indian plate during its northward flight from Gondwana to Asia. *Gondwana Res.,* **23,** 238–267.

Chen, J.S., Huang, B.C. & Sun, L.S., 2010. New constraints to the onset of the India-Asia collision: paleomagnetic reconnaissance on the Linzizong Group in the Lhasa Block, China. *Tectonophysics.,* **489,** 189–209.

Chen, J.S., Huang, B.C., Yi, Z.Y., Yang, L.K. & Chen, L.W., 2014. Paleomagnetic and ^{40}Ar/^{39}Ar geochronological results from the Linzizong Group, Linzhou Basin, Lhasa Terrane, Tibet: implications to paleogene paleolatitude and onset of the India-Asia collision. *J. Asian Earth Sci.,* **96,** 162–177.

Chen, W.W. *et al.*, 2012. Paleomagnetic results from the early cretaceous Zenong Group volcanic rocks, Cuoqin, Tibet, and their paleogeographic implications. *Gondwana Res.,* **22**(2), 461–469.

Chen, W.W. *et al.*, 2017. Combined paleomagnetic and geochronological study on Cretaceous strata of the Qiangtang terrane, central Tibet. *Gondwana Res.,* **41,** 373–389.

Chen, Y., Cogné, J.P., Courtillot, V., Tapponnier, P. & Zhu, X.Y., 1993. Cretaceous paleomagnetic results from western Tibet and tectonic implications. *J. geophys. Res.,* **98,** 17 981–17 999.

Cheng, X., Zhou, Y.N., Guo, Q., Hou, B.N. & Wu, H.N., 2015. Paleomagnetism of triassic rocks in the western Lhasa terrane, Tibetan Plateau, and its tectonic implications. *Geol. Bull. China.,* **34,** 306–317. (in Chinese).

Cogné, J.P., 2003. PaleoMac: a MacintoshTM application for treating paleomagnetic data and making plate reconstructions. *Geochem. Geophys. Geosyst.,* **4,** 1007. doi: 10.1029/2001GC000227.

Dannemann, S., Appel, E., Rösler, W., Neumann, U., Liebke, U. & Nag, D., 2022. Paleomagnetic indication for India-Asia collision at 12°N and maximum 810 km Greater India extent in the western suture zone. *Geophys. J. Int.,* **229,** 1193–1211.

Day, R., Fuller, M. & Schmidt, V., 1977. Hysteresis properties of titanomagnetites: grain-size and compositional dependence. *Phys. Earth planet. Inter.,* **13,** 260–267.

Deng, C.L., Mitchell, R.N. & Wang, W.T., 2023. Editorial preface to special issue: continental evolution and sedimentary basins of the Tibetan Plateau and its environs. *Glob. Planet. Change,* **226,** doi:10.1016/j.gloplacha.2023.104161.

Ding, J.K. *et al.*, 2015. Paleomagnetism of the oligocene Kangtuo Formation red beds (Central Tibet): inclination shallowing and tectonic implications. *J. Asian Earth Sci.,* **104,** 55–68.

Dong, X.B., Wang, Z.M., Tan, C.Z., Yang, H.X., Cheng, L.R. & Zhou, Y.X., 1991. New results of paleomagnetic studies of the Qinghai-Tibet Plateau. *Geol. Rev.,* **37,** 160–164. (in Chinese).

Dunlop, D., Özdemir, Ö., Clark, D. & Schmidt, P., 2000. Time–temperature relations for the remagnetization of pyrrhotite (Fe_7S_8) and their use in estimating paleotemperatures. *Earth planet Sci. Lett.,* **176,** 107–116.

Dunlop, D.J., 2002. Theory and application of the day plot (M_{rs}/M_s versus H_{cr}/H_c) 2. Application to data for rocks, sediments, and soils. *J. geophys.Res.,* **107**(B3), EPM 5–1-EPM 5-15.

Dupont-Nivet, G., Lippert, P.C., van Hinsbergen, D.J.J., Meijers, M.J.M. & Kapp, P., 2010. Palaeolatitude and age of the Indo-Asia collision: palaeomagnetic constraints. *Geophys. J. Int.,* **182,** 1189–1198.

Enkin, R.J., 1990. Formation et Déformation de l'Asie Depuis la Fin de Lère Primaire: Les apports de l'étude paléomagnétique des formations secondaires de Chine du Sud, *PhD thesis*, Univ. de Paris 7, Paris, 333pp.

Fisher, R.A., 1953. Dispersion on a sphere. *Phi. Trans. R. Soc. A,* **217**(1130), 295–305.

Font, E., Rapalini, A.E., Tomezzoli, R.N., Trindade, R.I.F. & Tohver, E., 2012. Episodic remagnetizations related to tectonic events and their consequences for the South America Polar Wander Path. *Geol. Soc., Lond., Spec. Publ,* **371,** 55–87.

Froelich, P.N. *et al.*, 1979. Early oxidation of organic matter in pelagic sediments of the eastern equatorial Atlantic: suboxic diagenesis. *Geochim. Cosmochim. Acta.,* **43,** 1075–1090.

Fu, Q. *et al.*, 2022. Remagnetization of the Jurassic limestones in the Zaduo Area, Eastern Qiangtang Terrane (Tibetan Plateau, China): implications for the India–Eurasia collision. *Geophys. J. Int.,* **228,** 2073–2091.

Gao, L., Wang, Q.F., Deng, J., Chen, F.G., Zhang, S.H. & Yang, Z.Y., 2019. Magmatic-hydrothermal alteration mechanism for Late mesozoic remagnetization in the South China Block. *J. geophys. Res.,* **124,** 10 704–10 720.

Guo, Q., 2009. Research on paleomagnetism of Gangdise plate of Qinghai-Tibet Plateau in late Paleozoic. Master thesis, Northwest Universtiy, Xi'an, Shanxi, pp. 1–60. (in Chinese).

Guo, Z.T. *et al.*, 2002. Onset of Asian desertification by 22 Myr ago inferred from loess deposits in China. *Nature,* **416,** 159–163.

Harlan, S.S., Geissman, J.W., Snee, L.W. & Reynolds, R.L.,1996. Late Cretaceous remagnetization of proterozoic mafic dikes, southern Highland Mountains, southwestern Montana: a paleomagnetic and ^{40}Ar/^{39}Ar study. *Geol. Soc. Am. Bull.,* **108**(6), 653–668.

Hu, X.M., Ma, A.L., Xue, W.W., Garzanti, E., Cao, Y., Li, S.M., Sun, G.Y. & Lai, W., 2022. Exploring a lost ocean in the Tibetan Plateau: birth, growth, and demise of the Bangong-Nujiang Ocean. *Earth Sci. Rev.,* **229,** doi:10.1016/j.earscirev.2022.104031.

Hu, X.M., Wang, J.G., BouDagher-Fadel, M., Garzanti, E. & An, W., 2016. New insights into the timing of the India-Asia collision from the Paleogene Quxia and Jialazi formations of the Xigaze forearc basin, south Tibet. *Gondwana Res.,* **32,** 76–92.

Huang, W., Dupont-Nivet, G., Lippert, P.C., Van Hinsbergen, D.J. & Hallot, E., 2013. Inclination shallowing in Eocene Linzizong sedimentary rocks from Southern Tibet: correction, possible causes and implications for reconstructing the India–Asia collision. *Geophys. J. Int.,* **194**(3), 1390–1411.

Huang, W.T. *et al.*, 2015. Paleolatitudes of the Tibetan Himalaya from primary and secondary magnetizations of Jurassic to lower Cretaceous sedimentary rocks. *Geochem. Geophys. Geosyst.,* **16,** 77–100.

Huang, W.T. *et al.*, 2017a. Remagnetization of the paleogene Tibetan himalayan carbonate rocks in the Gamba area: implications for reconstructing the lower plate in the India-Asia collision. *J. geophys. Res.,* **122,** 808–825.

Huang, W.T. *et al.*, 2017b. Remagnetization of carbonate rocks in southern Tibet: perspectives from rock magnetic and petrographic investigations. *J. geophys. Res.,* **122,** 2434–2456.

Huang, W.T., Jackson, M.J., Dekkers, M.J., Zhang, Y., Zhang, B., Guo, Z.J. & Dupont-Nivet, G., 2019. Challenges in isolating primary remanent magnetization from Tethyan carbonate rocks on the Tibetan Plateau: insight from remagnetized Upper Triassic limestones in the eastern Qiangtang block. *Earth planet Sci. Lett.,* **523,** 115695.

Jackson, M. & Swanson-Hysell, N.L., 2012. Rock magnetism of remagnetized carbonate rocks: another look. *Geol. Soc., Lond., Spec. Publ,* **371,** 229–251.

Jadoon, U.F., Huang, B.C., Shah, S.A., Rahim, Y., Khan, A.A. & Bibi, A., 2022. Multi-stage India-Asia collision: paleomagnetic constraints from Hazara-Kashmir syntaxis in the western Himalaya. *Geol. Soc. Am. Bull.,* **134,** 1109–1128.

Ji, C.J., Wu, Z.H., Yi, H.S., Xia, G.Q., Zhao, Z. & Wang, T., 2019. ^{13}C-^{18}O isotopic anomalous study of the carbonate rock at the Wenbudangsang PTB section, Tibet. *Acta Geol. Sin.,* **92,** 2018–2027. (in Chinese).

Ji, Z.S. *et al.*, 2018. Stratigraphic progress of the Coqen Basin and redefinition of the upper Permian-Jurassic stratigraphic sequence. *Acta Geosci. Sin.,* **39,** 401–407. (in Chinese).

Ji, Z.S., Yao, J.X. & Wu, G.C., 2007. Stratigraphic division of the marine Triassic in the Coqen area, western Gangdise, Tibet, China. *Geol. Bull. China.,* **26,** 947–952. (in Chinese).

Jiao, X.W. *et al.*, 2023. Middle Jurassic paleolatitude of the Tethyan Himalaya: new insights into the evolution of the Neo-Tethys Ocean. *J. geophys. Res.,* **128,** e2023JB026659.

Kapp, P. & DeCelles, P.G., 2019. Mesozoic–Cenozoic geological evolution of the Himalayan-Tibetan orogen and working tectonic hypotheses. *Am. J. Sci.,* **319,** 159–254.

Kapp, P., Murphy, M.A., Yin, A., Harrison, T.M., Ding, L. & Guo, J.H., 2003. Mesozoic and Cenozoic tectonic evolution of the Shiquanhe area of western Tibet. *Tectonics,* **22**(4), doi:10.1029/2001TC001332.

Katz, B., Elmore, R.D., Cogoini, M., Engel, M.H. & Ferry, S., 2000. Associations between burial diagenesis of smectite, chemical remagnetization, and magnetite authigenesis in the Vocontian trough, SE France. *J. geophys. Res.,* **105**(B1), 851–868.

Kent, D.V., 1985. Thermoviscous remagnetization in some Appalachian limestones. *Geophys. Res. Lett.,* **12,** 805–808.

Kirschvink, J.L., 1980. The least-squares line and plane and the analysis of palaeomagnetic data. *Geophys. J. Int.,* **62,** 699–718.

Kruiver, P.P., Dekkers, M.J. & Heslop, D., 2001. Quantification of magnetic coercivity components by the analysis of acquisition curves of isothermal remanent magnetization. *Earth planet Sci. Lett.,* **189**(3–4), 269–276.

Li, S. *et al.*, 2022c. New paleomagnetic results of the upper cretaceous to lower eocene sedimentary rocks from the Xigaze forearc basin and their tectonic implications. *Tectonophysics,* **837,** doi:10.1016/j.tecto.2022.229433.

Li, S., Guilmette, C., Ding, L., Xu, Q., Fu, J.J. & Yue, Y.H., 2017b. Provenance of mesozoic clastic rocks within the Bangong-Nujiang suture zone, central Tibet: implications for the age of the initial Lhasa-Qiangtang collision. *J. Asian Earth Sci.,* **147,** 469–484.

Li, S., Li, Y.L., Tan, X.D., Meng, J., Shang, Y.M., Wei, Y.S. & Wang, C.S., 2020. Paleomagnetism and microtextures reveal Neohimalayan deformation pattern in the northwestern Tethys Himalaya. *J. Asian Earth Sci.,* **202,** doi:10.1016/j.jseaes.2020.104516.

Li, S., Yin, C.Q., Guilmette, C., Ding, L. & Zhang, J., 2019. Birth and demise of the Bangong-Nujiang Tethyan Ocean: a review from the Gerze area of central Tibet. *Earth Sci. Rev.,* **198,** doi:10.1016/j.earscirev.2019.102907.

Li, Z.Y. *et al.*, 2022b. Jurassic true polar wander recorded by the Lhasa terrane on its northward journey from Gondwana to Eurasia. *Earth planet Sci. Lett.,* **592,** doi:10.1016/j.epsl.2022.117609.

Li, Z.Y., Ding, L., Laskowski, A.K., Burke, W.B., Chen, Y., Song, P.P., Yue, Y.H. & Xie, J., 2022a. New paleomagnetic constraints on the early cretaceous paleolatitude of the Lhasa terrane (Tibet). *Earth Sci. Front.,* **10,** doi:10.3389/feart.2022.785726.

Li, Z.Y., Ding, L., Lippert, P.C., Song, P.P., Yue, Y.H. & van Hinsbergen, D.J.J., 2016. Paleomagnetic constraints on the mesozoic drift of the Lhasa terrane (Tibet) from Gondwana to Eurasia. *Geology,* **44**(9), 727–730.

Li, Z.Y., Ding, L., Song, P.P., Fu, J.J. & Yue, Y.H., 2017a. Paleomagnetic constraints on the paleolatitude of the Lhasa block during the early Cretaceous: implications for the onset of India-Asia collision and latitudinal shortening estimates across Tibet and stable Asia. *Gondwana Res.,* **41,** 352–372.

Liebke, U., Appel, E., Ding, L., Neumann, U., Antolin, B. & Xu, Q., 2010. Position of the Lhasa terrane prior to India-Asia collision derived from palaeomagnetic inclinations of 53 Ma old dykes of the Linzhou Basin: constraints on the age of collision and post-collisional shortening within the Tibetan Plateau. *Geophys. J. Int.,* **182,** 1199–1215.

Lin, J.L. & Watts, D.R., 1988. Paleomagnetic results from the Tibetan Plateau. *Phi. Trans. R. Soc., A,* **327,** 239–262.

Lippert, P.C., van Hinsbergen, D.J.J. & Dupont-Nivet, G., 2014. Early Cretaceous to present latitude of the central proto-tibetan Plateau: a paleomagnetic synthesis with implications for cenozoic tectonics, paleogeography, and climate of Asia, in *GSA Special Papers: Toward an Improved Understanding of Uplift Mechanisms and the Elevation History of the Tibetan Plateau,* Vol. **507,** pp. 1–21, eds Nie, J., Horton, B.K. & Hoke, G.D., Geological Society of America.

Liu, Y.C. *et al.*, 2022. Paleomagnetism of the late cretaceous Jingzhushan Formation red beds on the northern margin of the Lhasa terrane in the Qinghai-Tibet Plateau and its tectonic significance. *Prog. Geophys.,* **37,** 2275–2290. (in Chinese).

Lowrie, W., 1990. Identification of ferromagnetic minerals in a rock by coercivity and unblocking properties. *Geophys. Res. Lett.,* **17,** 159–162.

Ma, Y.M. *et al.*, 2014. Paleomagnetism and U-Pb zircon geochronology of lower Cretaceous lava flows from the western Lhasa terrane: new constraints on the India-Asia collision process and intracontinental deformation within Asia. *J. geophys. Res.,* **119**(10), 7404–7424.

Ma, Y.M. *et al.*, 2017. Paleomagnetic and geochronologic results of latest Cretaceous lava flows from the Lhasa terrane and their tectonic implications. *J. geophys. Res.,* **122,** 8786–8809.

Ma, Y.M. *et al.*, 2018. A stable southern margin of Asia during the Cretaceous: paleomagnetic constraints on the Lhasa-Qiangtang collision and the maximum width of the Neo-Tethys. *Tectonics,* **37,** 3853–3876.

Ma, Y.M. *et al.*, 2019. Paleomagnetic constraints on the origin and drift history of the North Qiangtang terrane in the Late Paleozoic. *Geophys. Res. Lett.,* **46,** 689–697.

Ma, Y.M. *et al.*, 2022a. Location of the Lhasa terrane in the Late Cretaceous and its implications for crustal deformation. *Palaeogeogr. Palaeoclimatol. Palaeoecol.,* **588,** doi:10.1016/j.palaeo.2021.110821.

Ma, Y.M. *et al.*, 2022b. Jurassic paleomagnetism of the Lhasa terrane—implications for Tethys evolution and true polar wander. *J. geophys. Res.,* **127,** e2022JB025577.

McCabe, C. & Channell, J.E.T., 1994. Late paleozoic remagnetizatio in limestones of the Craven Basin (northern England) and the rock magnetic fingerprint of remagnetized sedimentary carbonates. *J. geophys. Res.,* **99,** 4603–4612.

McCabe, C. & Elmore, R.D., 1989. The occurrence and origin of late Paleozoic remagnetization in the sedimentary rocks of North America. *Rev. Geophys.,* **27,** 471–494.

Meert, J.G. *et al.*, 2020. The magnificent seven: a proposal for modest revision of the van der Voo (1990) quality index. *Tectonophysics,* **790**(15), 228549.

Meng, J. *et al.*, 2017. Reduced convergence within the Tibetan Plateau by 26 ma? *Geophys. Res. Lett.,* **44,** 6624–6632.

Meng, J., Wang, C.S., Zhao, X.X., Coe, R., Li, Y.L. & Finn, D., 2012. India-Asia collision was at 24°N and 50 Ma: palaeomagnetic proof from southernmost Asia. *Sci. Rep.,* **2,** doi:10.1038/srep00925.

Niu, C. *et al.*, 2023. The cretaceous stationary Lhasa terrane constrained by the paleolatitude of 103 ma volcanic rocks from the Nima area. *Glob. Planet. Change,* **220,** doi:10.1016/j.gloplacha.2022.103998.

Otofuji, Y. *et al.*, 2007. Spatial gap between Lhasa and Qiangtang blocks inferred from middle Jurassic to Cretaceous paleomagnetic data. *Earth planet Sci. Lett.,* **262,** 581–593.

Paterson, G.A., Zhao, X., Jackson, M. & Heslop, D., 2018. Measuring, processing, and analyzing hysteresis data. *Geochem. Geophys. Geosyst.,* **19**(7), 1925–1945.

Pick, T. & Tauxe, L., 1994. Characteristics of magnetite in submarine basaltic glass. *Geophys. J. Int.,* **119,** 116–128.

Pozzi, J.P., Westphal, M., Zhou, Y.X., Xing, L.S. & Chen, X.Y., 1982. Position of the Lhasa block, South Tibet, during the late Cretaceous. *Nature,* **297,** 319–321.

Pullaiah, G., Irving, E., Buchan, K. & Dunlop, D., 1975. Magnetization changes caused by burial and uplift. *Earth planet Sci. Lett.,* **28,** 133–143.

Ran, B. *et al.*, 2017. Kinematics of the crust around the Tanggula Shan in North–Central Tibet: constraints from paleomagnetic data. *Gondwana Res.,* **48,** 124–133.

Ran, B., Wang, C.S., Zhao, X.X., Li, Y.L., He, M., Zhu, L.D. & Coe, R.S., 2012. New paleomagnetic results of the early Permian in the Xainza area, Tibetan Plateau and their paleogeographical implications. *Gondwana Res.,* **22,** 447–460.

Raterman, N.S., Robinson, A.C. & Cowgill, E.S., 2014. Structural and detrital zircon geochronology of the Domar fold-thrust belt: evidence of pre-cenozoic crustal thickening of the western Tibetan Plateau. *Geol. Soc. Am. Spec Paper,* **507,** 89–114.

Raymo, M.E. & Ruddiman, W.F., 1992. Tectonic forcing of late Cenozoic climate. *Nature,* **359,** 117–122.

Roberts, A.P., 2015. Magnetic mineral diagenesis. *Earth Sci. Rev.,* **151,** 1–47.

Roberts, A.P., Florindo, F., Chang, L., Heslop, D., Jovane, L. & Larrasoaña, J.C., 2013. Magnetic properties of pelagic marine carbonates. *Earth Sci. Rev.,* **127,** 111–139.

Roberts, A.P., Tauxe, L., Heslop, D., Zhao, X. & Jiang, Z., 2018. A critical appraisal of the "Day" diagram. *J. geophys. Res.,* **123,** 2618–2644.

Song, P.P., Ding, L., Lippert, P.C., Li, Z.Y., Zhang, L.Y. & Xie, J., 2020. Paleomagnetism of middle triassic lavas from northern Qiangtang (Tibet): constraints on the closure of the Paleo-Tethys Ocean. *J. geophys. Res.,* **125,** e2019JB017804.

Su, T. *et al.*, 2019. Uplift, climate and biotic changes at the Eocene-Oligocene transition in Southeast Tibet. *Nat. Sci. Rev.,* **6,** 495–504.

Suk, D., Peacor, D. & Van der Voo, R., 1990. Replacement of pyrite framboids by magnetite in limestone and implications for palaeomagnetism. *Nature,* **345,** 611–613.

Sun, G.Y., Hu, X.M. & Sinclair, H.D., 2017. Early Cretaceous palaeogeographic evolution of the Coqen Basin in the Lhasa Terrane, southern Tibetan Plateau. *Palaeogeogr. Palaeoclimatol. Palaeoecol.,* **485,** 101–118.

Sun, Z.M., Jiang, W., Li, H.B., Pei, J.L. & Zhu, Z.M., 2010. New paleomagnetic results of paleocene volcanic rocks from the Lhasa block: tectonic implications for the collision of India and Asia. *Tectonophysics,* **490,** 257–266.

Sun, Z.M., Jiang, W., Pei, J.L. & Li, H., 2008. New early Cretaceous paleomagnetic data from volcanic of the eastern Lhasa Block and its tectonic implications. *Acta Petrol. Sin.,* **24,** 1621–1626. (in Chinese).

Sun, Z.M., Pei, J.L., Li, H.B., Xu, W., Jiang, W., Zhu, Z.M., Wang, X.S. & Yang, Z.Y., 2012. Palaeomagnetism of late Cretaceous sediments from southern Tibet: evidence for the consistent palaeolatitudes of the southern margin of Eurasia prior to the collision with India. *Gondwana Res.,* **21,** 53–63.

Tan, X.D., Gilder, S., Kodama, K.P., Jiang, W., Han, Y.L., Zhang, H., Xu, H.H. & Zhou, D., 2010. New paleomagnetic results from the Lhasa block: revised estimation of latitudinal shortening across Tibet and implications for dating the India-Asia collision. *Earth planet Sci. Lett.,* **293,** 396–404.

Tang, X.D., Huang, B.C., Yang, L.K., Yi, Z.Y., Qiao, Q.Q. & Chen, L.W., 2013. Paleomagnetism and Ar-Ar geochronology of Cretaceous volcanic rocks in the middle Lhasa terrane, China and tectonic implications. *Chinese J. Geophys.,* **56**(1), 136–149. (in Chinese).

Tong, Y.B., Yang, Z.Y., Pei, J.L., Li, J.F., Jin, S.C., Hou, L.F., Sun, X.X. & Zhang, Z.J., 2022. New late Cretaceous paleomagnetic results from the Lhasa terrane and their implications for the suturing of India and Eurasia and the closure of the Neo-Tethys Ocean. *Geol. Soc. Am. Bull.,* **134,** 3242–3257.

Tong, Y.B., Yang, Z.Y., Pei, J.L., Wang, H., Xu, Y.C. & Pu, Z.W., 2017. Paleomagnetism of the Upper Cretaceous red-beds from the eastern edge of the Lhasa Terrane: new constraints on the onset of the India-Eurasia collision and latitudinal crustal shortening in southern Eurasia. *Gondwana Res.,* **48,** 86–100.

Van der Voo, R. & Torsvik, T.H., 2012. The history of remagnetization of sedimentary rocks: deceptions, developments and discoveries. *Geol. Soc., Lond., Spec. Publ.,* **371,** 23–53.

van Hinsbergen, D.J.J., Lippert, P.C., Dupont-Nivet, G., McQuarrieh, N., Doubrovine, P.V., Spakman, W. & Torsvik, T.H., 2012. Greater India Basin hypothesis and a two-stage Cenozoic collision between India and Asia. *Proc. Natl. Acad. Sci. U.S.A.,* **109,** 7659–7664.

van Hinsbergen, D.J.J., Lippert, P.C., Li, S.H., Huang, W.T., Advokaat, E.L. & Spakman, W., 2018. Reconstructing Greater India: paleogeographic, kinematic, and geodynamic perspectives. *Tectonophysics,* **760,** 69–94.

Wang, S. *et al.*, 2022. Paleomagnetic and geochronological results of the Risong Formation in the western Lhasa Terrane: insights into the Lhasa-Qiangtang collision and stratal age. *Palaeogeogr. Palaeoclimatol. Palaeoecol.,* **586,** doi:10.1016/j.palaeo.2021.110778.

Wang, S. *et al.*, 2023. New Middle Jurassic paleomagnetic and geochronologic results from the Lhasa terrane: contributions to the closure of the Meso-Tethys Ocean and Jurassic true polar wander. *Geophys. Res. Lett.,* **50,** e2023GL103343.

Weil, A.B. & Van der Voo, R., 2002. Insights into the mechanism for orogen-related carbonate remagnetization from growth of authigenic Fe-oxide: a scanning electron microscopy and rock magnetic study of devonian carbonates from northern Spain. *J. geophys. Res.,* **107**(B4), 1–14.

Wu, G.C. *et al.* 2018. The early triassic conodonts in Rendo area of Zhongba county, Tibet, and paleogeographic pattern of the West Gangdise block in early Triassic. *Acta Geosci. Sin.,* **39,** 409–418 (in Chinese).

Wu, G.C., Ji, Z.S., Trotter, J.A., Yao, J.X. & Zhou, L.Q., 2014. Conodont biostratigraphy of a new permo-Triassic boundary section at Wenbudangsang, north Tibet. *Palaeogeogr. Palaeoclimatol. Palaeoecol.,* **411,** 188–207.

Xu, Y.C., Tan, X.D., Li, S., Li, Y.L., Ran, B., Han, Y.L., Sun, J.P. & Ma, Z.N., 2022. Paleomagnetism of the greater Indian passive margin sediments from the upper Cretaceous succession: evidence for long-delayed remagnetizations and implication for the India-Asia collision. *J. Asian Earth Sci.,* **229,** doi:10.1016/j.jseaes.2022.105165.

Yan, M.D., Zhang, D.W., Fang, X.M., Ren, H.D., Zhang, W.L., Zan, J.B., Song, C.H. & Zhang, T., 2016. Paleomagnetic data bearing on the mesozoic deformation of the Qiangtang Block: implications for the evolution of the paleo- and meso-Tethys. *Gondwana Res.,* **39,** 292–316.

Yang, T.S. *et al.*, 2015a. New insights into the India-Asia collision process from Cretaceous paleomagnetic and geochronologic results in the Lhasa terrane. *Gondwana Res.,* **28,** 625–641.

Yang, T.S. *et al.*, 2015b. Paleomagnetic results from the Early Cretaceous Lakang Formation lavas: Constraints on the paleolatitude of the Tethyan Himalaya and the India-Asia collision. *Earth planet Sci. Lett.,* **428,** 120–133.

Ye, X.H. & Li, J.F., 1987. Palaeomagnetism and evolution of Tibet plates and tethys. *J. Chengdu Coll. Geol.,* **14,** 65–79. (in Chinese).

Yi, Z.Y., Huang, B.C., Chen, J.S., Chen, L.W. & Wang, H.L., 2011. Paleomagnetism of early paleogene marine sediments in southern Tibet, China: implications to onset of the India–Asia collision and size of Greater India. *Earth planet Sci. Lett.,* **309,** 153–165.

Yi, Z.Y., Huang, B.C., Yang, L.K., Tang, X.D., Yan, Y.G., Qiao, Q.Q., Zhao, J. & Chen, L.W., 2015. A quasi-linear structure of the southern margin of Eurasia prior to the India-Asia collision: first paleomagnetic constraints from upper Cretaceous volcanic rocks near the western syntaxis of Tibet. *Tectonics,* **34,** 1431–1451.

Yi, Z.Y., Wang, T.Y., Meert, J.G., Zhao, Q. & Liu, Y.S., 2021. An initial collision of India and Asia in the equatorial humid belt. *Geophys. Res. Lett.,* **48,** e2021GL093408.

Yi, Z.Y., Yang, S.L., Meert, J.G. & Ma, X.X., 2023. Paleomagnetism of late Cretaceous dykes in the Gangdese belt: new constraints on the position and structure of the southern margin of Asia prior to the India-Asia collision. *China Geol,* **6,** 269–284.

Yin, A. & Harrison, T.M., 2000. Geologic evolution of the Himalayan-Tibetan orogeny. *Ann. Revs. Earth planet. Sci.,* **28**(1), 211–280.

Yu, L. *et al.*, 2022. Remagnetization of carboniferous limestone in the Zaduo Area, Eastern Qiangtang Terrane, and its tectonic implications. *Earth Sci. Front.,* **10,** doi:10.3389/feart.2022.825943.

Yuan, J. *et al.*, 2021. Rapid drift of the Tethyan Himalaya terrane before two-stage India-Asia collision. *Natl. Sci. Rev.,* **8,** 173.

Yuan, J. *et al.*, 2022. Triple-stage India-Asia collision involving arc-continent collision and subsequent two-stage continent-continent collision. *Glob. Planet. Change,* **212,** doi:10.1016/j.gloplacha.2022.103821.

Zhang, M. *et al.*, 2021. Magnetostratigraphy across the end-Permian mass extinction event from the Meishan sections, southeastern China. *Geology,* **49**(11), 1289–1294.

Zhang, S., 2016. Origin and reservoir characteristics of dolomite of the Upper Permian in Coqen basin, Tibet. *PhD thesis*, Chengdu University of Technology, Chengdu, China, pp. 1–113. (in Chinese).

Zhang, Y. *et al.*, 2020. Fluid migration and widespread remagnetization in the Dabashan fold and thrust belt, China. *J. geophys. Res.,* **125,** e2020JB019989.

Zhang, Y., Jia, D., Yin, H.W., Liu, M.C., Xie, W.R., Wei, G.Q. & Li, Y.X., 2016. Remagnetization of lower Silurian black shale and insights into shale gas in the Sichuan Basin, south China. *J. geophys. Res.,* **121,** 491–505.

Zhou, L.Q., 2012. In-situ SHRIMP oxygen isotopic study on conodonts from the Permian/Triassic boundary of Wenbudangsang Section, Tibet. *Master thesis*, Chengdu University of Technology, Chengdu, China, pp. 1–70. (in Chinese).

Zhou, Y.N. *et al.*, 2016. Paleomagnetic study on the Triassic rocks from the Lhasa Terrane, Tibet, and its paleogeographic implications. *J. Asian Earth Sci.,* **121,** 108–119.

Zhu, D.C., Zhao, Z.D., Niu, Y.L., Dilek, Y., Hou, Z.Q. & Mo, X.X., 2013. The origin and Pre-Cenozoic evolution of the Tibetan Plateau. *Gondwana Res.,* **23,** 1429–1454.

Zhu, Z.W., Zhu, X.Y. & Zhang, Y.M., 1981. Palaeomagnetic observation in Xizang and Continental Drift. *Acta Geophys. Sin.,* **24,** 40–49. (in Chinese).

Zijderveld, J.D.A., 1967. A.C. demagnetization of rocks: analysis of results, in *Methods in Paleomagnetism,* pp. 254–286, eds Collinson, D.W., Creer, K.M. & Runcorn, S.K., Elsevier.